RSC Advances

PAPER

View Article Online
View Journal | View Issue

Cite this: *RSC Adv.*, 2025, **15**, 41447

Novel Schiff base Cu(II) and Au(III) complexes: spectroscopic, computational, and electrochemical insights for H_2O_2 sensor applications

Manara A. Ayoub,*[ab] Asmaa M. Fahim [c] and Hend S. Magar *[d]

A Schiff base ligand, called (*E*)-2-((1*H*-pyrrol-2-yl)methyleneamino) benzenethiol (H_2L), was synthesized from 2-aminothiophenol and pyrrole-2-carbaldehyde; the copper(II) and gold(III) coordination complex were then successfully synthesized and characterized by elemental analysis, FT-IR, UV-vis, NMR, XRD, SEM, TGA/DTA and conductivity measurements. Based on spectroscopic and structural data, ligand H_2L behaves as a tridentate ligand to Cu(II) *via* its thiophenolic sulfur, azomethine nitrogen and pyrrolic nitrogen atoms, and as a bidentate ligand to Au(III) *via* sulfur and azomethine nitrogen. Density Functional Theory (DFT/B3LYP/LANL2DZ) studies provided additional information on molecular orbital, electronic reactivity, charge distributions, and thermodynamic stability and showed that the gold(III) half-sandwich complex was more exothermic, favoring thermodynamic stability, because of the stronger Au–ligand based on covalency and relativistic orbital interactions. Electrochemical analysis using screen-printed electrodes (SPEs) modified with H_2L/Cu and H_2L/Au nanomaterials showed significantly improved electron-transfer kinetics and capacitive behavior, with the H_2L/Au system exhibiting the lowest charge-transfer resistance (19 Ω) and highest specific capacitance (774 F g^{-1}). The H_2L/Au-modified electrode also exhibited excellent electrocatalytic activity for non-enzymatic hydrogen peroxide sensing, with a wide linear range (0.05–1725 μM), ultra-low detection limit (0.025 μM), high sensitivity, and outstanding stability. The practical applicability of the H_2L/Au-modified electrode was demonstrated with real-sample analysis of water, milk, cheese salami, and juice, showing excellent recovery of hydrogen peroxide in each sample. In summary, the combination of Schiff base coordination chemistry and transition-metal centers resulted in multifunctional nanocomposites with high thermal and electrochemical stability, making them suitable nanomaterials for possible energy-storage devices and electrochemical biosensors.

Received 4th September 2025
Accepted 23rd October 2025

DOI: 10.1039/d5ra06669g

rsc.li/rsc-advances

1. Introduction

Schiff bases have played a prominent role as chelating ligands in transition metal coordination chemistry due to their remarkable stability under both oxidative and reductive conditions. Similar to imine ligands, they exhibit intermediate donor characteristics between hard and soft Lewis bases, enabling versatile coordination with a wide range of metal ions.[1,2]

Schiff base metal complexes incorporating nitrogen and sulfur donor atoms are important due to their adaptable coordination behavior, sensitivity, ease of synthesis, and selectivity. These complexes have found applications as intermediates in biological systems, as well as catalysts in chemical reactions and stabilizers in polymer materials.[3] Transition metal complexes bearing Schiff-base ligands with SNN donor sets have been extensively investigated as effective catalysts in a range of organic redox reactions and electrochemical reduction processes.[4–7] The Schiff base complex derived from 2-aminothiophenol and pyrrole-2-carbaldehyde integrates the functional characteristics of both thiophenol and pyrrole moieties, offering the potential to yield novel materials with broad applicability. Further investigations into its structural features, as well as its biological and catalytic properties, may uncover valuable new insights and expand its utility across various fields.[8] Cyclic voltammetry provides valuable information not only on the thermodynamics of redox processes but also on the kinetics of heterogeneous electron transfer and coupled chemical reactions.[9,10] Hydrogen peroxide (H_2O_2) is a widely studied analyte due to its strong oxidizing properties and its presence in a variety of household and industrial products, including cosmetics, dyes, disinfectants, lacquers, and shampoos. Biologically, H_2O_2 is a common byproduct of enzymatic reactions catalyzed by oxidases. Elevated levels of

[a]*Chemistry Department, Faculty of Science, Taibah University, Al Madinah Al Munawarah, 41411, Saudi Arabia. E-mail: manara_2005@yahoo.com*
[b]*Chemistry Department, Faculty of Women for Arts, Science and Education, Ain-Shams University, Cairo, 11757, Egypt*
[c]*Department of Green Chemistry, National Research Centre, Dokki, P. O. 12622, Cairo, Egypt*
[d]*Applied Organic Chemistry Department, National Research Centre, Dokki, P.O. Box.12622, Giza, Egypt. E-mail: hendamer2000@yahoo.com*

H_2O_2 in the human body are linked to oxidative stress, a key contributor to the pathogenesis of several disorders, including Alzheimer's disease, cancer, diabetes, Huntington's disease, Parkinson's disease, and general disruptions in cellular homeostasis. Various analytical techniques have been employed for the detection of H_2O_2, such as electrochemical methods, colorimetric assays, and fluorescence-based approaches. Among these, electrochemical detection[11,12] has gained increasing attention due to its high sensitivity, simplicity, rapid response, and suitability for real-time monitoring,[13–16] rapid analysis,[17–19] cost-effectiveness, high sensitivity,[20–22] and ability to support real-time monitoring.[23–25] Notably, enzyme-free electrochemical sensors[26,27] offer a promising solution to overcome limitations associated with enzyme-based detection systems.[23,28–31] Significant efforts have been directed toward the development of supercapacitors[32] advanced energy storage technologies to meet the growing demand for sustainable energy, largely driven by environmental concerns and the impacts of climate change. Among these technologies, electrical capacitors particularly supercapacitors have emerged as promising candidates, owing to their high energy storage capacity, long cycle life, and rapid charging–discharging capabilities. In light of the ongoing global energy crisis, exacerbated by rapid population growth and economic expansion, the need for efficient, reliable, and scalable energy storage systems especially for use in portable electronics and renewable energy applications is more pressing than ever.

In recent years, advances in electrochemical techniques have markedly enhanced the field of analytical chemistry, owing to their exceptional sensitivity,[13,22,29] selectivity,[13,16,17,21] and cost-effectiveness.[17,18,21]The utilization of electroanalytical techniques offers a relatively brief analysis duration in comparison to other methods. Furthermore, these technicalities are also applied in the identification of reaction mechanisms.[33,34] The complexes of copper(II) and gold(III) represent a significant category in the field of chemistry, notable not only for their intriguing coordination chemistry, which includes flexible redox properties, geometry, and oxidation states[35] but also for their wide-ranging applications in diverse areas, including their role as catalysts in oxidation, reduction, and epoxidation reactions.[36]

While Schiff base complexes of Cu(II) and Au(III) have been extensively studied, most previous reports focus on their synthesis and basic characterization, often examining only one metal center in isolation. In contrast, the present work offers a comparative study of Cu(II) and Au(III) complexes derived from the same Schiff base ligand, enabling a direct evaluation of how the metal center influences structural, electronic, and electrochemical behavior. Furthermore, this study uniquely combines spectroscopic, electrochemical, and DFT computational methods to provide a holistic understanding of these complexes. Importantly, their application in hydrogen peroxide (H_2O_2) sensing is explored for the first time, revealing notable performance, particularly for the Cu(II) complex, thus positioning these complexes as promising candidates for electrochemical sensor platforms.

The focus of this work is to create a new Schiff base ligand using 2-aminothiophenol and pyrrole-2-carbaldehyde, and subsequently its Cu(II) and Au(III) complexes. Structural elucidation of the ligand and its complexes involved comprehensive characterization techniques such as spectroscopy, thermogravimetric analysis, and microscopy; this was supported by DFT and (TD-DFT) computational investigations. The work will also develop a better understanding of the electrochemical characteristics of the ligand and its complexes as possible electrode modifiers in supercapacitors and as a sensing platform for hydrogen peroxide using a non-enzymatic process; the design, synthesis, and electrochemical data will also be validated with the analysis of real-sample validated data following the production of the ligand from analyzing the performance.

2. Experimental

2.1. Materials, instruments and methods

All chemicals used were of analytical grade (Merck or Sigma) and employed without further purification. Potassium chloride, potassium ferricyanide, potassium ferrocyanide, potassium mono- and dihydrogen phosphate, hydrogen peroxide, sodium hydroxide (NaOH), and hydrochloric acid (HCl) were all procured from Sigma-Aldrich. Microanalysis of carbon, hydrogen, nitrogen, and sulfur (CHNS) was performed using a PerkinElmer 2400 Elemental analyzer. Fourier-transform infrared (FTIR) spectra, prepared as KBr discs, were recorded on a Shimadzu 8000 FTIR spectrometer. Conductivity measurements in dimethylformamide (DMF) solution (1×10^{-3} M) at 25 °C were obtained using a HANNA HI 3512 instrument. Electronic absorption spectra within the 200–800 nm range were recorded with a PerkinElmer Lambda 35 UV-vis spectrophotometer. Thermoanalytical studies, including thermogravimetric analysis (TGA) and derivative thermogravimetry (DrTGA), were conducted under a nitrogen atmosphere over the temperature range of 25–900 °C at a heating rate of 10 °C min^{-1} using a Shimadzu TGA-50H thermal analyzer. Proton nuclear magnetic resonance (^{1}H-NMR) spectra were acquired on a Varian 300 MHz spectrometer. Sonication was performed with a Branson ultrasonic bath (B12; 220/240 V, 50/60 Hz, 4 A). Powder X-ray diffraction (XRD) analysis was carried out using a Shimadzu XRD-7000 diffractometer (Japan) with Cu Kα radiation ($\lambda = 1.5418$ Å) operated at 40 kV and 30 mA. Melting points were determined using a STUART SMP11 apparatus (Japan). Electrochemical and Supercapacitor measurements were performed with a CHI potentiostat using screen-printed electrodes (SPEs). For electrode modification, 10 mg of the synthesized material was dispersed in 1 mL of distilled water in an Eppendorf tube and sonicated for 30 minutes to obtain a homogeneous suspension. Subsequently, 10 μL of this suspension was drop-cast onto the SPE surface and allowed to dry at room temperature. Cyclic voltammetry (CV) and electrochemical impedance spectroscopy (EIS) were conducted in a solution containing 0.1 M KCl and 0.005 M ferro/ferricyanide $[Fe(CN)_6]^{3-/4-}$, as depicted inScheme 1.

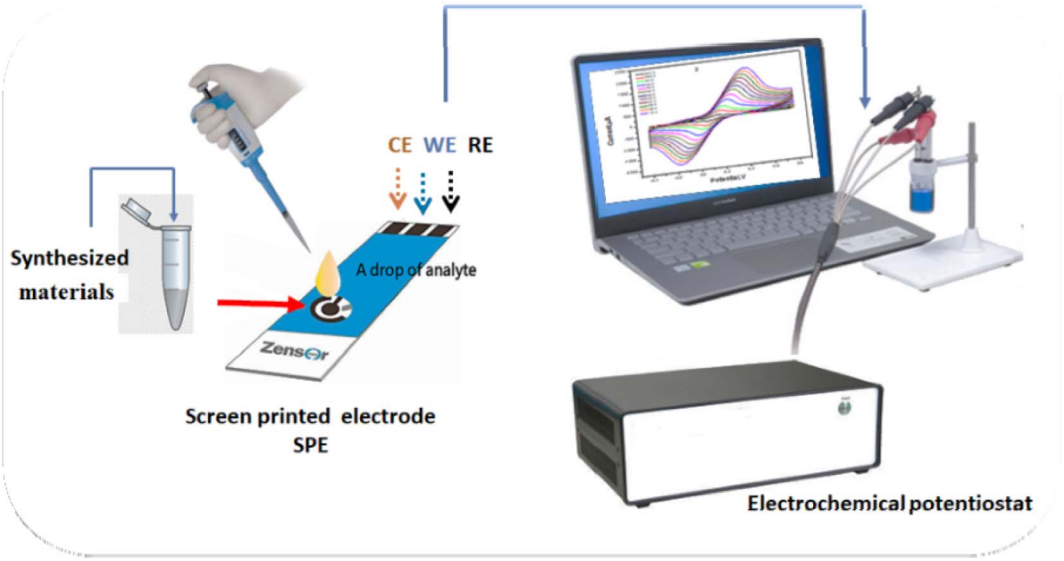

Scheme 1 The preparation method for modified SPE and electrochemical detection method.

2.2. Synthesis of Schiff base ligand H_2L (*E*)-2-((1*H*-pyrrol-2-yl) methylene amino) benzenethiol

Pyrrole-2-carbaldehyde (1.09 g, 10 mmol) dissolved in 50 mL of ethanol was gradually added dropwise to a stirred solution of 2-aminothiophenol (1.09 mL, 10 mmol) in 50 mL of ethanol. The mixture was heated to reflux and maintained under continuous stirring for two hours, followed by ultrasonic irradiation. After cooling, the resulting dark brown precipitate was collected by filtration and purified by recrystallization from hot ethanol. The yield was 1.645 g (70%), with a melting point of 180–182 °C. The FTIR data (ν, cm^{-1}): 3352 (w, ν_{NH}, pyrrole); 2337 (w, ν_{SH}, thiophenolic); 3060 (w, ν_{C-H}, aromatic); 1606 (s, $\nu_{C=N}$, azomethine); 1468 (s, $\nu_{C=C}$, aromatic); 753 (s, ν_{C-S}, thiophenolic). ^{1}H-NMR (300 MHz, DMSO-d_6, δ, ppm): 5.51 (s, 1H, SH), 6.82–8.05 (m, 4H, aromatic protons), multiplet for 3H corresponding to pyrrole protons, 12.14 (s, 1H, NH). Elemental analysis calculated for $C_{11}H_{10}N_2S$: C, 65.33; H, 4.95; N, 13.86; S, 15.84%. Found: C, 65.25; H, 4.88; N, 13.55; S, 15.65%.

2.3. Synthesis of metal Schiff base complex

A solution of metal salts (1 mmol) in 50 mL of ethanol was added dropwise to a stirred solution of the ligand H_2L (1 mmol) in 50 mL of ethanol. The reaction mixture was refluxed for two hours, and was exposed to ultrasonic irradiation. Upon cooling, the colored product precipitated out and was collected by filtration. The solid was washed sequentially with cold ethanol (the low temperature reduces solubility of the complex itself, helping to retain it while removing soluble impurities) and diethyl ether (to removes non-polar impurities and facilitates rapid drying of the complex after washing) (see Scheme 2).

This procedure illustrates the synthesis of the Schiff base ligand (*E*)-2-((1*H*-pyrrol-2-yl)methylene amino)benzenethiol (H_2L) and its corresponding H_2L/Cu(II) and H_2L/Au(III) complexes.

2.4. Computational analysis

Density Functional Theory (DFT) calculations were performed for each compound using the B3LYP functional in combination with the LANL2DZ basis set. Geometry optimizations were carried out using the Berny algorithm within the Gaussian 09W software package. Visualization of all optimized structures was accomplished using GaussView.[37] Vibrational frequency computations were performed after geometry optimizations to verify that the optimized structures were the true minimum. The NBO software[38] A built-in Gaussian was utilized to perform natural bond analysis[39] using the ground-state geometries that were acquired. The electronic absorption spectra of the ligand and its metal complexes were estimated using the TD-DFT approach (in conjunction with the LANL2DZ basic set) to account for the effect of the solvent around the molecule. The values of E_{HOMO} and E_{LUMO} allowed us to calculate all fundamental parameters, while we obtained other parameters from files.

3. Results and discussion

3.1. Physical properties

The physical properties of the Schiff base ligand (H_2L) and its metal complexes, including melting point, color, and other characteristics, are summarized in Table 1. The complexes are intensely colored powders that decompose above 200 °C.

3.2. FTIR spectral analysis

The infrared spectra for the compounds under consideration, recorded within the range of 400–4000 cm^{-1}, assist in identifying the regions of absorption vibrations. The most important stretching modes include ν_{NH}, ν_{S-H}, $\nu_{C=N}$, $\nu_{C=C}$, ν_{C-N}, ν_{C-S}, ν_{M-O}, ν_{M-N}, ν_{M-S} and ν_{M-Cl}. Table 2 and Fig. 1, display the infrared spectra of the Schiff base ligand (H_2L) and its complexes. To identify the coordination sites that might be contributed to chelation, the IR spectra of the complexes and the free ligand

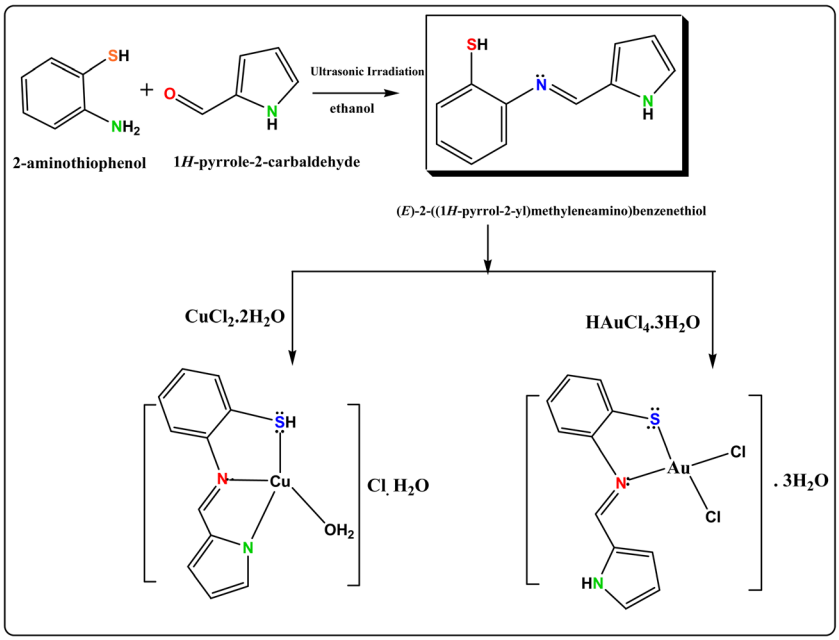

Scheme 2 Synthesis of the Schiff base ligand (*E*)-2-((1*H*-pyrrol-2-yl)methylene amino)benzenethiol (H_2L) and It's Cu(II) and Au(III) complexes.

Table 1 Physical and analytical data of the Schiff base H_2L and its metal complexes

				Elemental analyses, found (calcd.), (%)			
Ligand/complex molecular formula	Yield (%) *M* wt.	Color	M.p. (°C)	C	H	N	S
$H_2L(C_{11}H_{10}N_2S)$	(83) 202.06	Dark brown	180–182	65.25 (65.33)	4.88 (4.94)	13.55 (13.86)	15.65 (15.84)
$[Cu(HL)(H_2O)]Cl{\cdot}H_2O$ $(C_{11}H_{14}N_2O_2SClCu)$	(68) 337.06	brown	>220	39.22 (39.16)	4.27 (4.15)	8.13 (8.30)	9.15 (9.49)
$[Au(HL)(Cl_2)]{\cdot}3H_2O$ $(C_{11}H_{15}N_2O_3SCl_2Au)$	(65) 521.98	brown	>247	25.19 (25.29)	2.76 (2.87)	5.32 (5.36)	6.76 (6.13)

(H_2L) were compared. After chelation, it is expected that these peaks' positions and/or intensities will shift.[40] This band reveals the involvement of the azomethine nitrogen in interacting with metal ions by displaying a downward shift in the metal complexes' spectra.[41] The $\nu_{C=C}$ of the pyrrole and thiophenolic rings has been identified as the source of the bands that are apparent between 1566 and 1468 cm^{-1}. The C=C band, which exhibits increased intensity or broadening, frequently coincides with the shifted band. The bands appearing at 1247–1306 cm^{-1} have been assigned to ν_{C-N} mode.[42] The spectra of metal complexes has shifted a weak S–H band that was present at 2337 cm^{-1} in the case of the ligand.[43] However, the change of the $\nu_{sym(C-S)}$ from 753 cm^{-1} to lower or higher wave numbers in the complexes' spectra points to the SH group's involvement in chelation. The structure in Scheme 2, correctly depicts the presence of the NH moiety in the Schiff base ligand, which disappears due to deprotonation upon coordination to the Cu(II) center in the $[Cu(HL)(H_2O)]Cl.H_2O$ complex. However, the NH remains non-deprotonated upon coordination to the Au(III) center in the $[Au(HL)(Cl_2)]{\cdot}3H_2O$ complex.

The $\nu_{(C-H)asym}$ and $\nu_{(C-H)\ sym}$ appears in the region 2916–2838 cm^{-1}. The broad band at 3353–3379 cm^{-1} in the spectra of the complexes implies the presence of H_2O molecules. The band associated with the bending vibration of H_2O was identified within the range of 915–841 cm^{-1}.[44] The new bands at 420–449 cm^{-1} which is assignable to $\nu_{(M-S)}$ stretching vibration.[45] The $\nu_{(M-N)}$ mode has been ascribed to the bands that were seen at 534–561 cm^{-1}. It is determined that in the case of the Cu(II) complex, the H_2L ligand works as a tridentate ligand coordinated to the metal ions by means of thiophenolic S, azomethine N and pyrrole N, while in the case of the H_2L/Au(III) complex, the H_2L ligand behaves as a bidentate ligand coordinated to the metal ions through thiophenolic S, azomethine N.

3.3. ^{1}H-NMR and ^{13}C-NMR

The ^{1}H-NMR spectrum of the free Schiff base ligand H_2L is illustrated in Fig. 2. The signal observed at δ 5.51 ppm corresponds to the SH proton, whereas the signal at δ 12.14 is attributed to the NH proton. Additionally, the signal at δ 9.47 ppm is linked to the HC=N proton. The signals within the range of δ 6.82–8.05 ppm are associated with the aromatic protons of the thiophenolic and pyrrole rings. Furthermore, the ^{13}C NMR spectrum (*E*)-2-((1*H*-pyrrol-2- yl)methyleneamino) benzenethiol, recorded in DMSO-d^6, is illustrated in Fig. 3. The

Table 2 Characteristic infrared frequencies (cm^{-1}) of the Schiff base ligand H_2L and its H_2L/Cu and H_2L/Au complexes[a]

Ligand/complex	ν_{OH} (H_2O)	ν_{NH}	$\nu_{C-H\ Ar}$	$\nu_{(C-H)\ asym}$ / $\nu_{(C-H)\ sym}$	ν_{SH}	$\nu_{C=C\ Ar}$	ν_{C-S}	$\nu_{C=N}$	ν_{C-N}	ν_{M-N}	ν_{M-O}	ν_{M-S}	ν_{M-Cl}
H_2L $C_{11}H_{10}N_2S$		3352 (w)	3060 (w)	2937 w 2854 w	2337 (w)	1468 s	753 (s)	1606 (s)	1306 (m)	—	—	—	—
$[Cu(HL)(H_2O)]Cl\cdot H_2O$	3353 (m,br.)	—	3059 (w)	2926 s 2838 s	2323 (v.w)	1450m	760 (s)	1601 (v.s)	1247 (m)	561 (w)	473 (w)	449 (w)	—
$[Au(HL)(Cl_2)]\cdot 3H_2O$	3379 (m,br.)	3383 (w)	3064 (w)	2916 w 2844 w	2360 (v.w)	1462w	748 (w)	1591 (v.s)	1313 (w)	534 (w)	—	420 (w)	413 (w)

[a] s, strong; m, medium; br, broad; w, weak.

compound's carbon skeleton was revealed *via* the ^{13}C NMR spectrum. Notably, the carbon of the azomethine group located at position 2, 9 is the most de-shielded, resonating at δ 150.19 ppm. Additionally, the carbons that are adjacent to the nitrogen in the pyrrole ring at positions 11 and 14 are also deshielded, resonating at δ 135.88 and 116.52 ppm, respectively. The carbon of thiophenolic at position 6 appears at δ 131.62 ppm.

3.4. Electronic and magnetic measurement

The electronic absorption spectra of ligand H_2L and H_2L/Cu and H_2L/Au complexes in DMF solution were recorded at room temperature in the 200–800 nm wavelength range as indicated in Fig. 4 and Table 3. The formation of complexes is strongly supported by the observation of a shift in the bands in the spectra of all metal complexes. The bands detected in the range of (244–256 nm) for both of ligand H_2L and H_2L/Cu and H_2L/Au

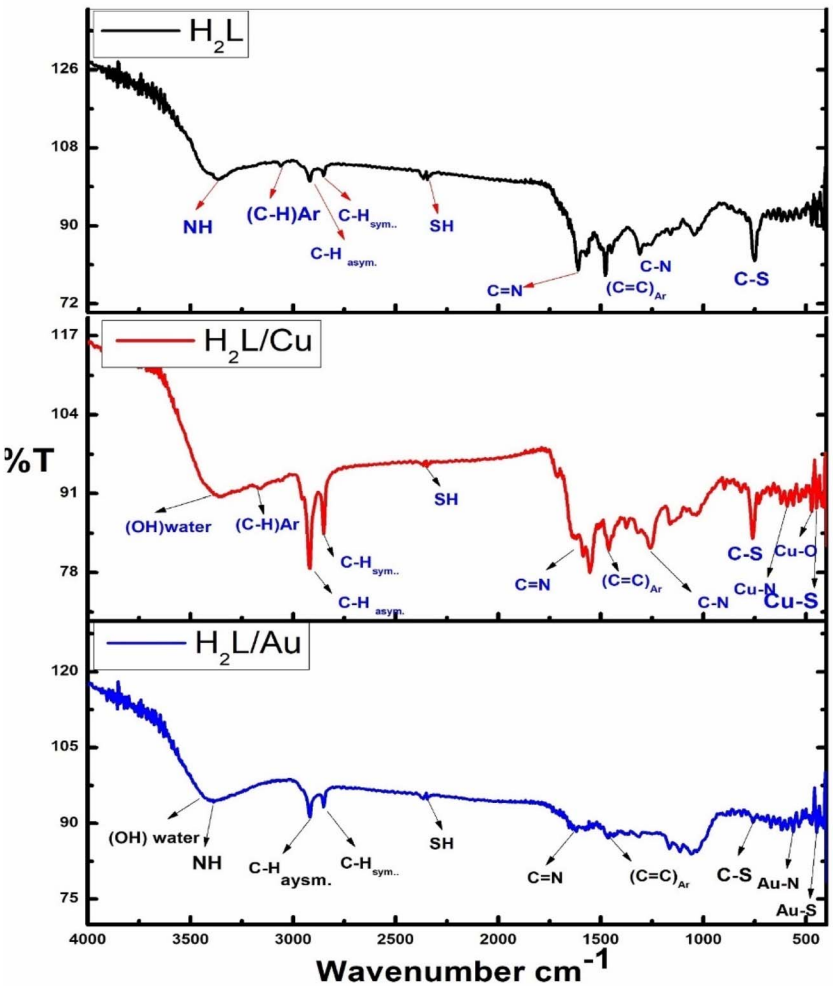

Fig. 1 Infrared spectra of ligand H_2L and its (H_2L/Cu) and (H_2L/Au) complexes.

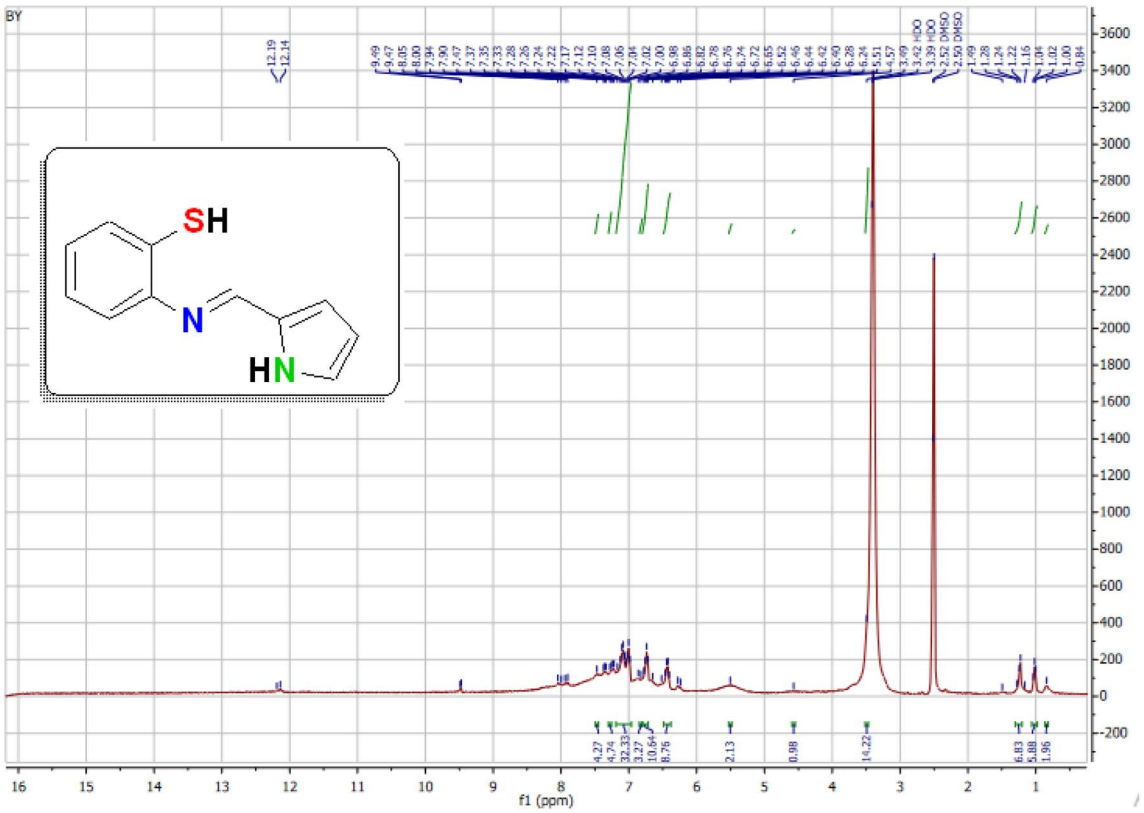

Fig. 2 ^{1}H-NMR of H_2L Schiff base ligand.

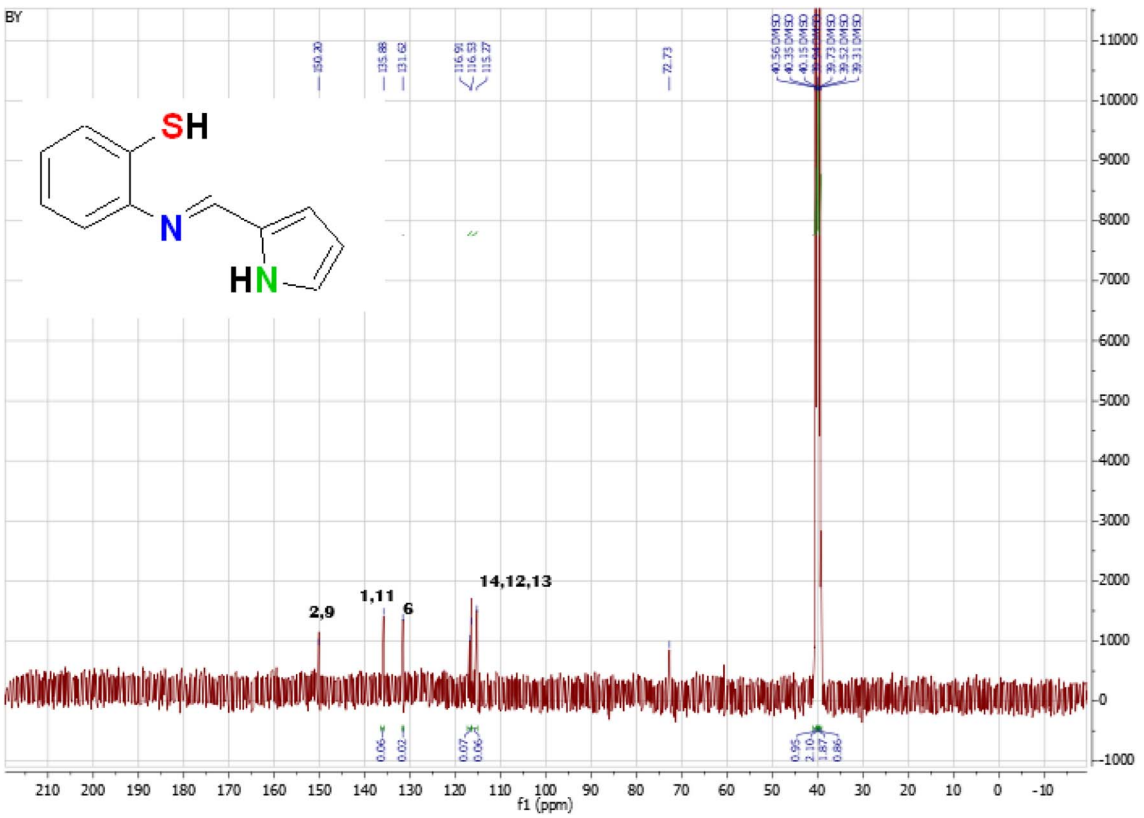

Fig. 3 ^{13}C-NMR spectrum (*E*)-2-((1*H*-pyrrol-2-yl) methylene amino) benzenethiol (H_2L).

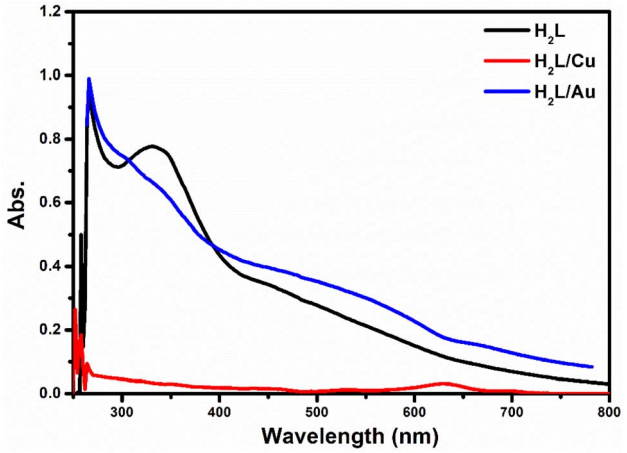

Fig. 4 Electronic spectra of Schiff base ligand H_2L and H_2L/Cu(II) and H_2L/Au(III) complexes.

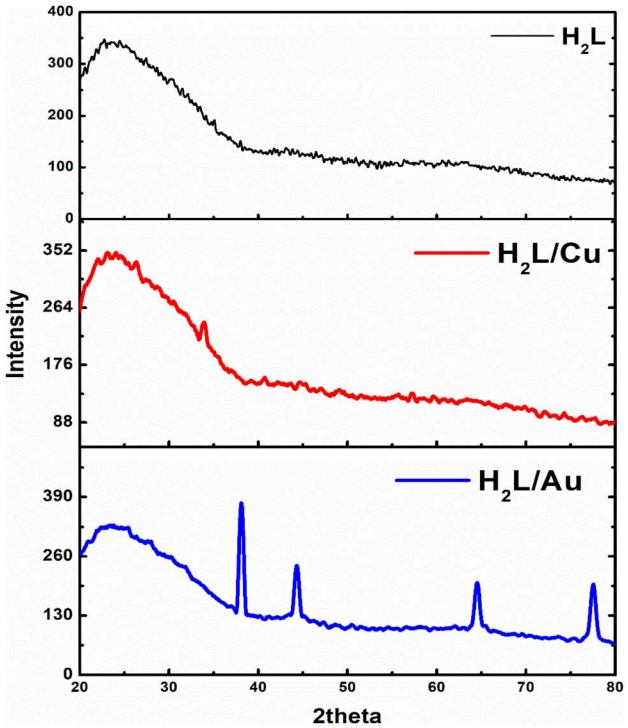

Fig. 5 X-Ray diffraction of Schiff base ligand (H_2L) and H_2L/Cu and H_2L/Au complexes.

complexes are ascribed to the intraligand π–π* transition of thiophenol and pyrrole rings.

The ligand and its metal complexes' spectral bands found in the 268–272 nm range are ascribed to n–π* transitions. In the case of complexes, the absorption band in the range of (340–346 nm) is ascribed to charge transfer (CT) transitions. Reports indicate that the metal can form dΠ–pΠ* bonds with ligands that have nitrogen as the donor atom. The metal ion possesses a vacant d orbital, allowing for ligand-to-metal (L → M) binding can occur when a pair of electrons from the ligand is accepted by the metal.[46] Electronic spectra of the H_2L/Cu complex displayed bands at 256, 286, 340, 532, and 630 nm, which are attributed to π → π* transition of thiophenol and pyrrole rings, n–π* transition of azomethine group, L→ Cu charge transfer, and d–d transitions. Electronic spectra of the H_2L/Au complex displayed bands at 244, 269, 346 nm may be attributed to π → π* transition of thiophenol and pyrrole rings, n–π* transition of azomethine group, and L → Au charge transfer, whereas the d–d transitions of H_2L/Au(III) complex are attributed to 500, 576, 676 nm.

3.5. Conductance measurement

A digital conductivity meter (model HANNA HI 3512 instrument) fitted with a dip-type cell with a cell constant of 1.0 cm^{-1} was used to measure the molar conductance. Freshly made 1×10^{-3} M solutions of the complexes in DMF at room temperature were used for the measurements. The conductance value recorded for the Cu(II) complex is 125 Ω^{-1} cm^2 mol^{-1}, indicating that this complex functions as a (1 : 1) electrolyte. On the other hand, the Au(III) complex exhibits non-electrolyte behavior value as indicated by its measured conductance value of 20.04 Ω^{-1} cm^2 mol^{-1}.[47]

3.6. X-ray diffraction

The patterns of X-ray powder diffraction for the ligand H_2L, as well as the H_2L/Cu and H_2L/Au complexes, are illustrated in Fig. 5. Upon examining these patterns, it is observed that the H_2L, the H_2L/Cu complex are amorphous and the H_2L/Au complex is well crystalline, respectively. The comprehensive data regarding diffraction, which includes angle ($2\theta^o$), interplanar spacing (d value, Angstrom), and relative intensity (%), full width at half maximum (FWHM) of the significant intensity peak and particle size have been computed in Table 4. The crystallite size can be attained from XRD patterns by utilizing the FWHM of the characteristic peaks in accordance with the Debye–Scherrer eqn (1).[48]

$$D = K\lambda/\beta \cos\theta \quad (1)$$

Table 3 Electronic spectral data (nm), and molar conductance of Schiff base ligand H_2L and its metal complexes

Compound	π → π* (nm)	n → π* (nm)	Charge transfer (nm)	d–d Transition (nm)	Molar conductance Ω^{-1} cm^2 mol^{-1}
H_2L	254	272	—	—	—
$[Cu(HL)(H_2O)]Cl \cdot H_2O$	256	268	340	532, 630	125
$[Au(HL)(Cl_2)] \cdot 3H_2O$	—	269	346	500, 576, 676	20.04

Table 4 The predicted powder XRD parameters of the H_2L and its complexes

Compound	2θ	FWHM	d (Å)	I intensity	D = crystallite size nm	Average nm
H_2L	30.24	1.52	2.95	54	5.41	12.84
	32	1.78	2.78	31	4.66	
	33.07	1	2.70	22	8.30	
$[Cu(HL)(H_2O)]Cl\cdot H_2O$	33.91	0.6333	2.64	55	13.15	21.41
	40.73	0.280	2.21	15	30.39	
	57.25	0.440	1.60	19	20.69	
$[Au(HL)(Cl_2)]\cdot 3H_2O$	38.12	0.324	2.36	100	26	23.60
	44.30	0.392	2.04	44	21.79	
	64.51	0.439	1.44	37	21.46	
	77.48	0.406	1.23	47	25.04	

In this context, D represents the particle size of the crystal gain, K denotes a constant (0.94 for Cu grid), λ signifies the X-ray wavelength (1.5406 Å), θ indicates the Bragg diffraction angle, and β refers to the integral peak width. The estimation of the particle size was based on the maximum intensity value in comparison to the other peaks. In Table 4 and Fig. 5, the XRD patterns of the H_2L ligand and the H_2L/Cu(II) complex are presented, both exhibiting several weak diffraction peaks of varying intensities. The average crystallite sizes of the H_2L ligand and the H_2L/Cu(II) complex were calculated to be 12.84 nm and 21.41 nm, respectively. The largest grain sizes, recorded at 8.30 nm for the H_2L ligand and 30.39 nm for the H_2L/Cu(II) complex, corresponded to diffraction angles of 33.04° and 40.73°, respectively. Conversely, the smallest grain sizes, 4.66 nm for the H_2L ligand and 13.15 nm for the H_2L/Cu(II) complex, were observed at diffraction angles of 32.00° and 33.91°, respectively. For the H_2L/Au(III) complex, the XRD pattern displayed multiple distinct peaks with varying intensities. The most intense diffraction peak, corresponding to the largest grain size of 26.00 nm, appeared at a diffraction angle of 38.12°, while the smallest grain size of 21.46 nm was associated with a diffraction angle of 64.51°. Overall, the broader and less intense diffraction peaks observed for the H_2L ligand and H_2L/Cu(II) complex indicate a lower degree of crystallinity, which can be attributed to weaker metal–ligand interactions and possible structural disorder. In contrast, the sharp and highly intense peaks of the H_2L/Au(III) complex confirm its crystalline nature, consistent with the formation of rigid square-planar geometries that promote higher crystallinity.

3.7. Thermogravimetric analysis of the complexes

TGA is a valuable tool for characterizing the thermal stability and decomposition behavior of these complexes, providing insights into their structure, bonding, and reactivity. The thermal stability of transition metal complexes is affected by various factors, such as the characteristics of the metal ion, the kind of ligand, and the coordination environment. Metal ions with higher charges and smaller ionic radii tend to form stronger bonds with ligands, leading to increased thermal stability. Ligands that form strong covalent bonds with metal ions, such as those containing nitrogen or sulfur donor atoms, also enhance thermal stability.[49,50]

The thermal characteristics of the target complexes were examined utilizing the TG/DTG method. The decomposition stages, temperature intervals, weight loss percentages, and the resulting decomposition products are detailed in Table 5, and Fig. 6. The thermal degradation of $[Cu(HL)(H_2O)]Cl\cdot H_2O$ occurs in three distinct stages. The initial decomposition stage is observed within the temperature range 25–125 °C resulting in a mass loss of 6.020 (calc. 5.340)% attributed to the release of one crystalline water molecule. The second one which is between 125 °C and 325 °C, has a mass loss of 28.870 (calc. 28.991%) which is equivalent to the loss of $1/2Cl_2$, coordinated water, C_3H_3. The third step falls between the 325 °C and 900 °C with exhibiting a mass loss of 56.593 (calc. 56.938)%. It is attributed to the loss of $2C_2H_2$, CH=N,$1/2N_2$, $1/2C_2$ &C_2. The total estimated mass loss is (calc./found %; 91.269/91.483%).

The thermal degradation of $[Au(HL)(Cl_2)]\cdot 3H_2O$ occurs in three distinct steps. The initial decomposition step is observed within the temperature range of 25–235 °C, resulting in a mass loss of 10.570 (calc. 10.345)% attributed to the release of three crystalline water molecules. The second step falls between 235 °C and 555 °C, exhibiting a mass loss of 42.610 (calc. 42.950%) which is attributed to the loss of Cl_2, $C_4H_4N_2$, C=N C_2H_2, $1/2H_2$, $1/2C_2$. The third step which is between 555 °C and 900 °C, has a mass loss of 13.820 (calc. 13.858%) which is the result of the loss of C_2, $1/2H_2$, $1/2C_2$, the total estimated mass loss is (calc./found %; 67.153/67.000%).

3.8. Morphological analysis

SEM studies were utilized to examine the shape, texture, aggregation, and physical state of the surfaces of compounds. Morphological analysis plays a vital role in classifying the distinct formation of coordination compounds. From Fig. 7A and B, morphology of the $[Cu(HL)(H_2O)]Cl.\ H_2O$, and $[Au(HL)(Cl_2)].\ 3H_2O$ complexes. It possesses a rock-like appearance and a substantial territorial area. These observations revealed the amorphous structure, which complicated interpretation because of its unclear appearance. The H_2L/Cu(II) complex exhibits a morphology composed of agglomerated, irregularly shaped particles. These particles appear loosely

Table 5 Thermoanalytical results (TGA, DTG) of Cu(II) and Au(III) complexes

Complex	Steps	Temperature range (°C)	DTG peak	TG weight loss, % Calcd	Found	Assignment
$[Cu(HL)(H_2O)]Cl\cdot H_2O$	1st	25–125	114	5.340	6.020	Loss of one lattice water
	2nd	125–325	199	28.991	28.870	Loss of 1/2 Cl_2, coordinated water, C_3H_3
			266			
	3rd	325–900	408	56.938	56.593	Loss of –CH═N, $2C_2H_2$, $1/2N_2$, C_2, $1/2C_2$
			575			
			736			
$[Au(HL)(Cl_2)]\cdot 3H_2O$	1st	25–235	65	10.345	10.570	Loss of three lattice water
			104			
	2nd	235–555	241	42.950	42.610	Loss of Cl_2, $C_4H_4N_2$, C═N C_2H_2, $1/2H_2$, $1/2C_2$
	3rd	555–900	557	13.858	13.820	Loss of C_2, $1/2H_2$, $1/2C_2$

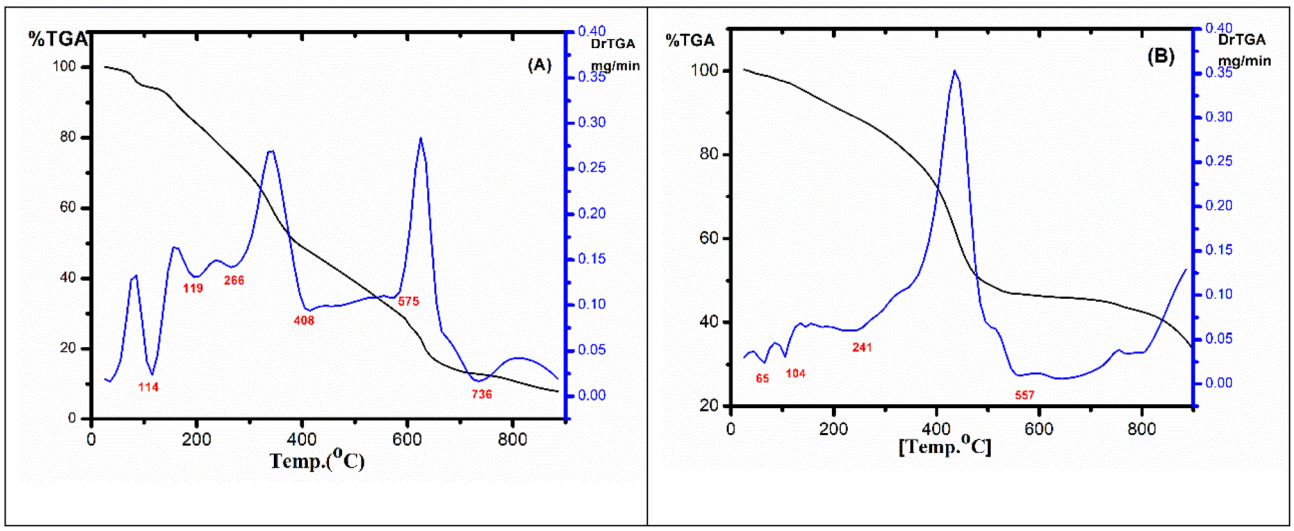

Fig. 6 TGA/DTG curves (A) $[Cu(HL)(H_2O)]Cl\cdot H_2O$ and (B) $[Au(HL)(Cl_2)]\cdot 3H_2O$.

distributed, randomly oriented, and loosely packed, displaying a rough surface texture. The absence of a well-defined geometry or ordered arrangement suggests a disordered and less controlled growth process. In contrast, the H_2L/Au(III) complex micrographs reveal distinct crystalline formations resembling overlapping sheets. These sheet-like structures appear stacked and interwoven, producing a layered morphology. The well-defined edges and smooth surfaces of the sheets indicate a more orderly and controlled crystal growth process, consistent with a higher degree of structural organization. To reinforce the morphological and compositional analysis of the synthesized complexes, we have performed Energy Dispersive X-ray Spectroscopy (EDS) and elemental mapping studies. The EDS spectra confirm the presence of the expected elements (Cu, Au, C, N, O, S, Cl) consistent with complex formation (see Fig. 7C and D).

3.9. Computational investigation

3.9.1. Physical identification of the H_2L and metal complexes. In this study, we optimized the HL and metal complexes using Gaussian (09)[51–54] through DFT/B3LYP/LANDZ2 basis set. Moreover, the physical characteristics used in the optimization of molecular structures of HL and metal complexes were concerning (σ) absolute softness,[55] (χ) electronegativities,[56] (ΔN_{max}) electronic charge,[57] (η) absolute hardness, (ω)[58] global electrophilicity,[59] (S) global softness,[60] and (Pi) chemical potential,[61] from the eqn (2)–(9) which were scheduled in Table 6 and Fig. 8.[53,62,63]

$$\Delta E = E_{LUMO} - E_{HOMO} \quad (2)$$

$$\chi = \frac{-(E_{HOMO} + E_{LUMO})}{2} \quad (3)$$

$$\eta = \frac{E_{LUMO} - E_{HOMO}}{2} \quad (4)$$

$$\sigma = 1/\eta \quad (5)$$

$$Pi = -\chi \quad (6)$$

$$S = 1/2\ \eta \quad (7)$$

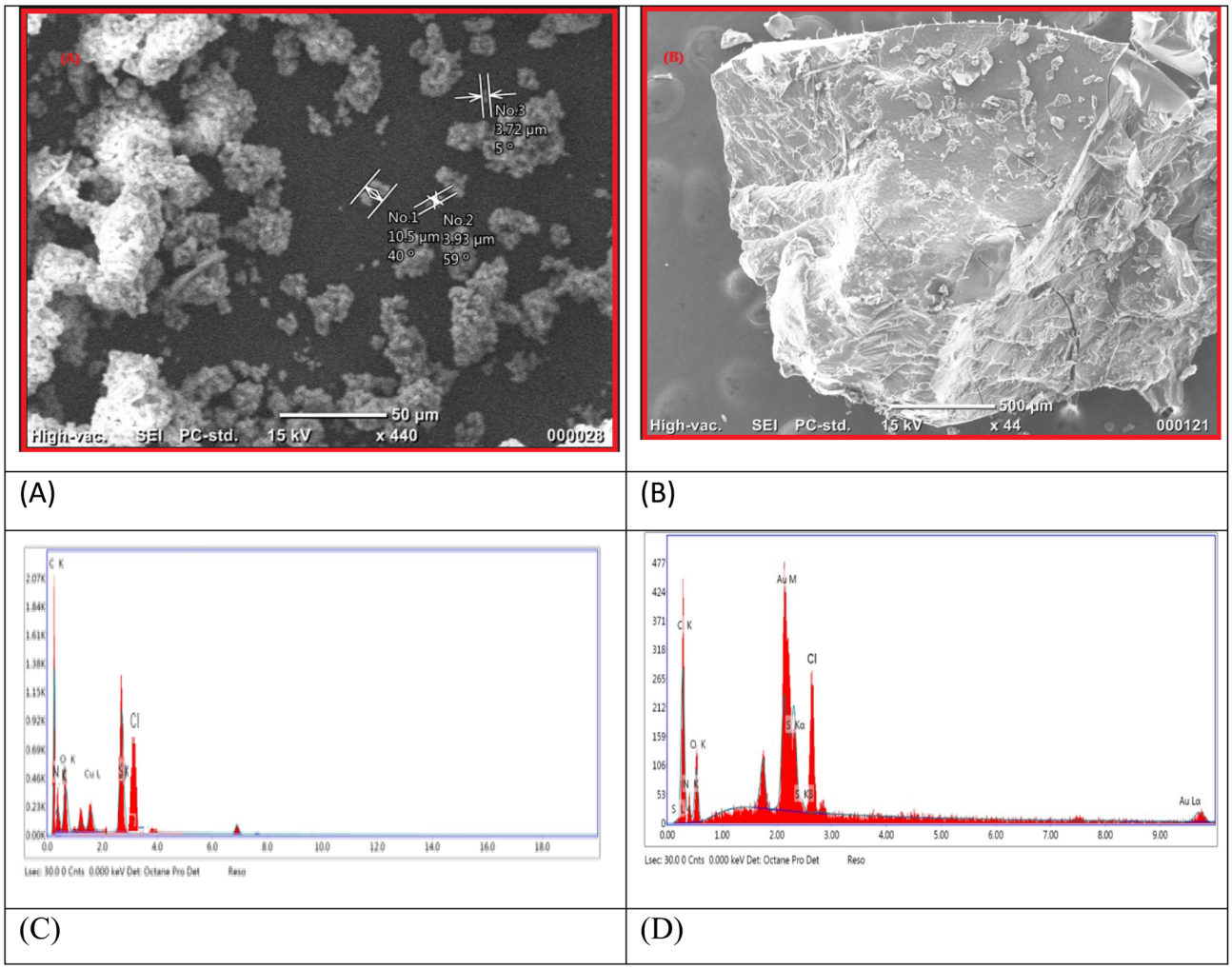

Fig. 7 SEM images of (A) [Cu (HL) (H_2O)] $Cl \cdot H_2O$ and (B) [Au (HL)(Cl_2)]$\cdot 3H_2O$. EDS spectra of (C) [Cu (HL) (H_2O)] $Cl \cdot H_2O$ and (D) [Au (HL)(Cl_2)]$\cdot 3H_2O$.

$$\omega = Pi^2/2 \quad (8)$$

$$\Delta N_{max} = -Pi/\eta \quad (9)$$

The optimized H_2L Ligand and H_2L/Cu, H_2L/Au complexes showed the non-planar structures which show the H_2L ligand with behavior typical of an organic molecule with moderate conjugation. Reactivity: it has been assigned a fairly high cell potential (3.50 eV) as it has the biggest band gap, which makes it 'hard', moderately stable, and not very reactive. Electron transfer: it also had the lowest electronegativity of the current ligands (3.62 eV), meaning it has the weakest motivation to attract electrons. As a more "neutral" molecule, it is not strongly an electron donor nor is it a strong electron acceptor. Polarity: the low dipole moment (1.03 D) adds to strong confirmation that it is not very polar. Moreover, the chelation with copper metal makes coordination to copper metal considerably contribute to the electronic properties. This showed the stability *vs.* reactivity band gap increased to 3.97 eV, resulting in the complex being more stable and harder than the free ligand. The coordination geometry around Cu(II) typically forms a stabilized electronic structure. Electronegativity increased to 4.02 eV, meaning it was pulling electrons strongly than the ligand. Polarity dipole moment

Table 6 Physical descriptors for compounds H_2L and metal complexes utilizing the DFT/B3LYP/LANL2DZ basis set

	H_2L	Cu complex	Au Complex
E_T (au)	−544.6249	−815.368	709.163
E_{HOMO} (eV)	−5.37	−6.00	−6.09
E_{LUMO} (e v)	−1.87	−2.03	−4.99
E_g (eV)	3.50	3.97	1.10
μ (D)	1.0313	5.1866	13.9761
χ (eV)	3.62	4.02	5.54
η (eV)	1.75	1.99	0.55
σ (eV)	0.57	0.50	1.82
Pi (eV)	−3.62	−4.02	−5.54
S (eV)	3.75	4.06	27.92
ω (eV)	2.07	2.02	10.07
ΔN_{max}	3.62	4.02	5.54

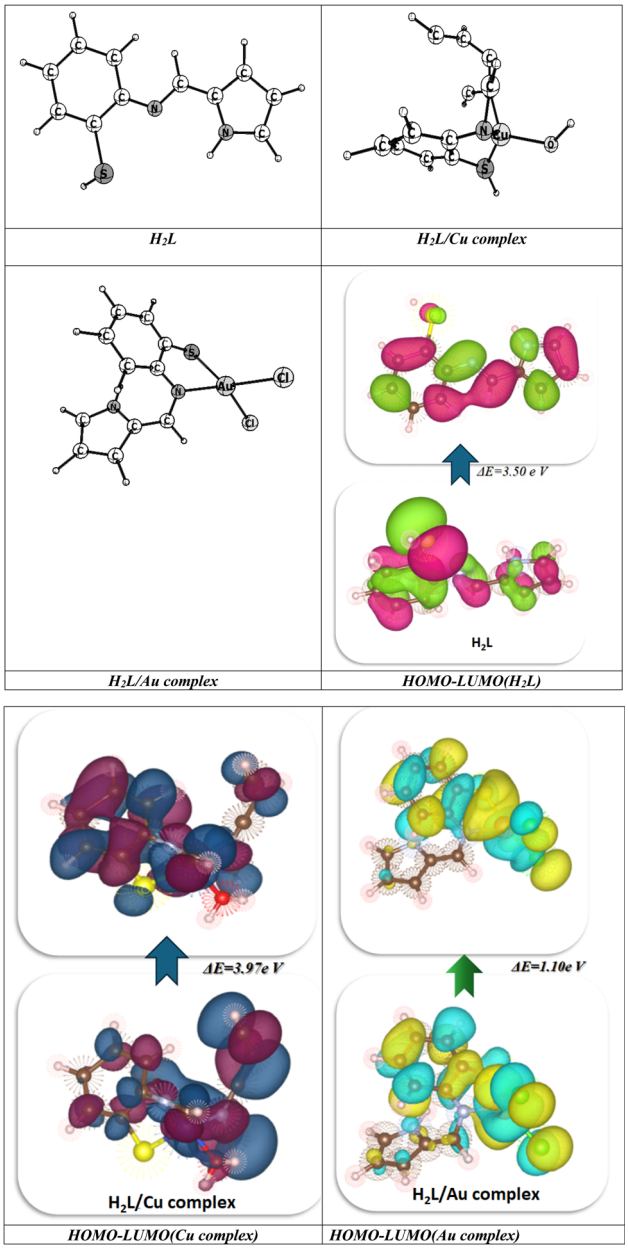

Fig. 8 Optimized structures and HOMO–LUMO energy of H_2L and its complexes.

increased substantially to 5.19 D, which we were expecting because coordination of a metal often increases asymmetrical and polar charge distribution, thus increasing potential solubility in polar solvents.[64,65] Moreover, H_2L/Au complex has radically different properties from applications of elementary metals, which are dominated by relativistic effects in gold atoms. Reactivity: the most pronounced feature is the very small band gap value of 1.10 eV. The gold complex is characterized as a very soft molecule; therefore, it is more polarizable, more reactive, and is expected to perform well in charge-transfer processes. This small gap is a hallmark of many gold catalysts and gold-related pharmaceuticals. Electron Affinity: the compound has very low (negative) LUMO energy (−4.99 eV), meaning it is a better electron acceptor. Electrophilicity: the complex has a very high electrophilicity index (27.92 eV) as well as, a very high electronegativity (5.54 eV), which plays a role in defining it as a strong electrophile with a propensity to seek electrons.[66,67] This is a common, useful feature that Lewis acid catalysts have. Polarity: it has the largest dipole moment (13.98 D) by a considerable distance, indicating an extremely polar molecular structure. So, we determined that the H_2L/Cu complex is the most stable and inert of the three. The H_2L/Au complex is the most reactive and polar, operating as a strong electrophile with its very small HOMO–LUMO gap. As such, it is a compelling candidate for utility in catalysis or materials science where reversible charge-transfer properties are important. The metal complexation process changes the electronic properties of the organic ligand to a very large extent, and the final chemical behavior is determined by the choice of metal (Cu *vs.* Au).

3.9.2. Mulliken charges of H_2L and metal complexes. Mulliken population data and electronic energies for your three compounds (ligand, Au complex, Cu complex). I will break this into three parts: (1) energies & dipoles, (2) Mulliken charges, (3) comparing legitimate insight as displayed in Fig. 9. First, I will discuss the H_2L ligand $E_{elec} = -544.62$ hartree dipole moment $\approx$ 1.74 D (moderate polarity), H_2L/Au complex: $E_{elec} = -709.16$ hartree, dipole moment $\approx$ 6.23 debye, much larger, which reflects strong metal coordination induced polarization. H_2L/Cu complex (open-shell, doublet): $E_{elec} = -1698.52$ hartree, dipole moment $\approx$ 7.08 debye, also strongly polarized, suggestive of considerable electric dipole generation for substantial charge density and spin localization asymmetry. The increase in dipole by metal binding shows that charge density on the ligand is redistributed significantly to create greater polarity, due to the consideration of coordination-induced polarization in the bonding process.[29,68] Moreover, the Mulliken charges of H_2L ITS charges are quite evenly distributed onto the C, N, O atoms on each of the ligands. Donor atoms (N, O) are slightly negatively charged ($\sim$−0.3 to −0.5 e), ready for coordination, H largely positively charged, C mostly neutral. The H_2L/Au complex has a near-neutral Mulliken charge (+0.008*e*), because LANL2DZ ECP treats all electronic behavior, including core electrons, implicitly. Coordinated N atoms acquire a significant negative charge ($\approx -0.51e$), indicating that electron density is being donated into Au's empty orbitals. Nearby carbons become slightly positive to counterbalance. Similarly, the H_2L/Cu complex has a Cu center that is also close to neutral in Mulliken ($\approx$+0.05*e*), but spin density (from the unpaired electron) is highly localized on Cu and near donor atoms. N atoms are back to being significantly negative, confirming they are coordinated. Some carbons (often near the donor sites) also have non-negligible spin density, which signals partial delocalization of the d-hole in Cu into the ligand's π-system. Mulliken tends to underpredict charges on metals due to overlap in terminology used for basis sets, to know donor atoms get more negative upon binding, and metals stay close to neutral in the Mulliken scheme which showed the donors (N, O, S): become more negative upon coordination (largest for the Au complex), reflects electron density donation into the metal center. Metals: nearly neutral Mulliken charge (typical of Mulliken with ECPs), but Cu

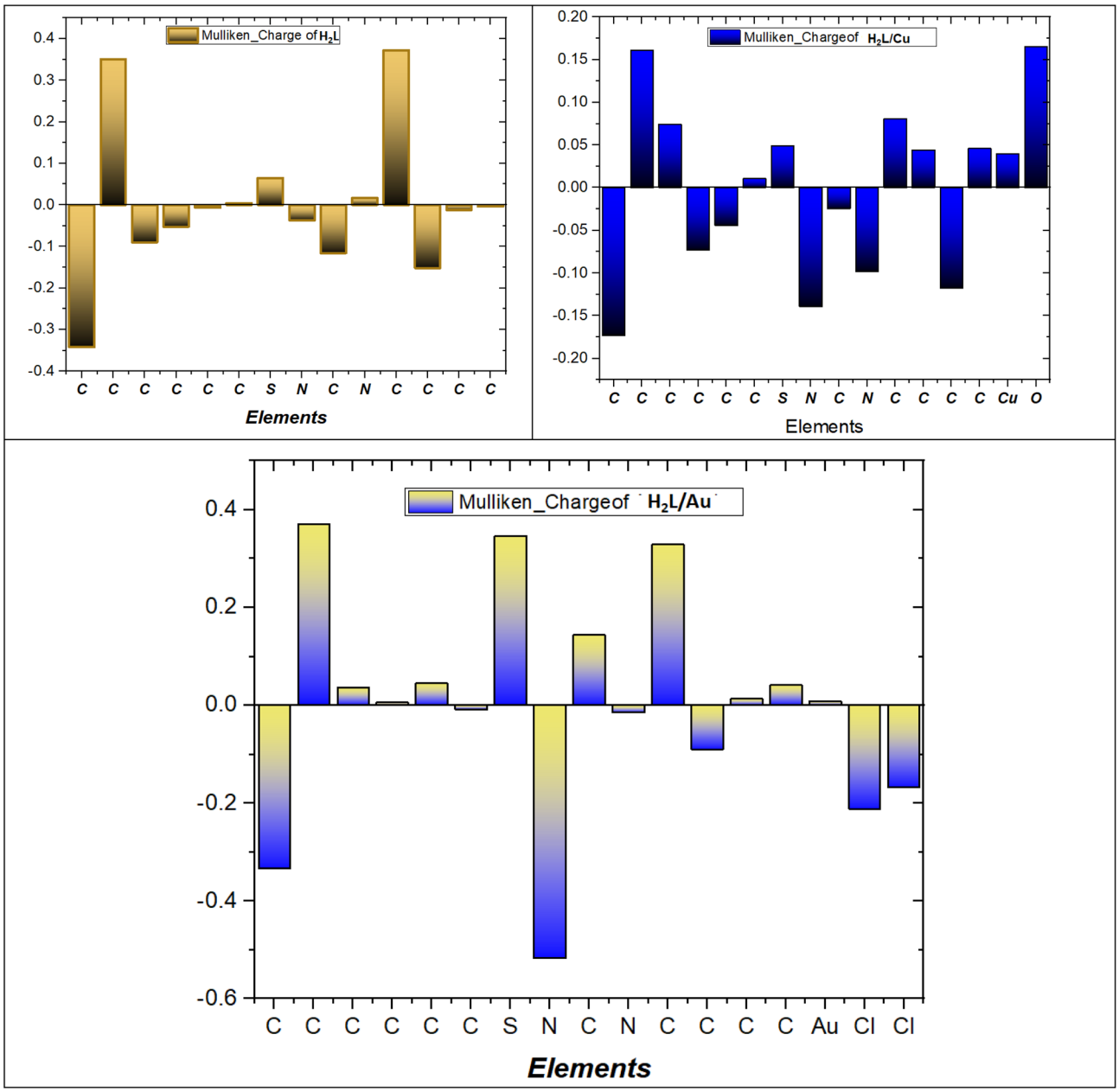

Fig. 9 Mulliken charge of H_2L, H_2L/Cu complex, and H_2L/Au complex.

shows a small positive sum, Au ~0. Carbons: compensate by showing a more positive net charge in the Au complex (due to ligand polarization). Halogens have a net negative charge in the Au complex, accounting for a larger dipole.

3.9.3. FT-IR analysis. The FT-IR spectrum overlay compares the free ligand H_2L ($C_{11}H_{10}N_2S$) with its H_2L/Cu(II) complex ($C_{11}H_{10}CuN_2OS$) to show the structural changes due to coordination. In the ligand, the strong C=N stretching at 1600–1650 cm^{-1} corresponds to the azomethine bond in free $C_{11}H_{10}N_2S$. In the complex $C_{11}H_{10}CuN_2OS$, this is reduced to slightly lower wavenumbers (≈1580–1630 cm^{-1}) due to azomethine coordination to copper. There are two new bands in the complex at ~450 cm^{-1} and ~500 cm^{-1} attributed to Cu–O, and Cu–N vibrations present in the complex but not in the free ligand, providing direct evidence of the formation of a metal–ligand bond. Finally, the complex displays a broad, strong band near 3200 cm^{-1} indicating an OH stretch, most likely related to the coordinated water molecule, or hydroxyl involvement, and both complexes keep their aromatic C–H stretching near 3050 cm^{-1}. Also, the C–S band near 750 cm^{-1} is retained in both, indicating that there is little contribution by sulfur. Overall, the spectral shifts and observed new peaks indicate that complexation has changed the vibrational environment, and confirms that coordination of Cu(II) with the ligand has been achieved (Fig. 10).

Analysis of the FT-IR spectrum of the H_2L/Au(III) complex ($C_{11}H_9AuCl_2N_2S$) provides defining vibrations indicative that

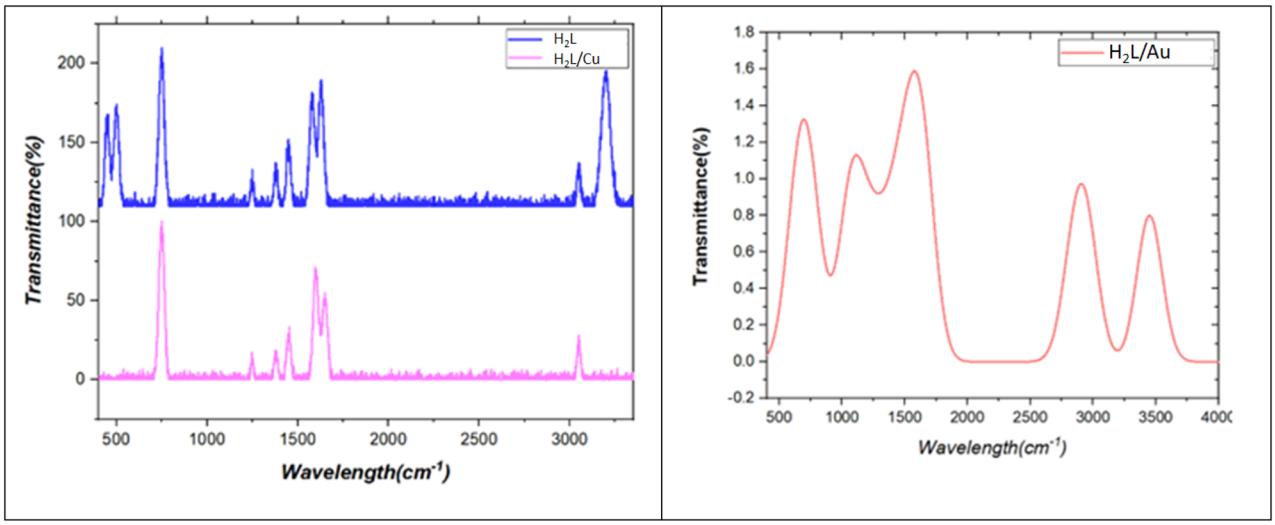

Fig. 10 Stimulated FT-IR of H_2L ligand, H_2L/Cu complex and H_2L/Au Complex.

metal–ligand coordination has occurred. The broad peaks in the 3400–3200 cm^{-1} region indicate possible N–H stretching vibrations, with weak bands between 3000 and 2800 cm^{-1} being C–H stretching due to the various aromatic and aliphatic functional groups present. The strong absorptions occurring in the region of 1650–1550 cm^{-1} were assigned the C=N and C=C stretching modes belonging to the heteroaromatic ligands. These bands are typically lower in wavenumber than the free ligand and are indicative of the coordination of the donors of the ligands to the Au center. Additional bands between 1300 and 1000 cm^{-1} correspond to C–N and C–S stretching vibrations, also affected by bonding to gold. In the low-frequency region, there are strong diagnostic absorptions between 500–400 cm^{-1} that are assigned to Au–S and Au–N stretches, which provide direct evidence of coordination through nitrogen and sulfur donor atoms. Weak bands near 350 cm^{-1} can be attributed to Au–Cl stretching if chloride ligands remain bound (Fig. 10). Overall, the spectrum shows that functional groups related to ligands such as C=N and S moieties cause a shift upon complexation, and Au–S, Au–N, and Au–Cl vibrations indicate that a stable gold coordination complex has formed.

3.9.4. TD-DFT analysis. Although the simulated UV-vis spectra for both compound 1(H_2L) ligand and the Cu complex display vastly different electronic transition activities consistent with differences in their electronic nature and configuration. Depicted in Fig. 11, H_2L ligand has intensely $\pi \rightarrow \pi^*$ transitions that dominate in its UV electronic spectra, especially between 250 and 400 nm, with additional contributions from $n \rightarrow \pi^*$ transitions, and a weak charge transfer (CT) transitions. These transitions involve excitation of an electronic transition in the π conjugated system and lone pair orbitals, which is similar to what we would expect from organic chromophores. In contrast, the H_2L/Cu complex gives rise to a markedly broadened spectra allowing long wavelengths to emerge in the visible region. In the UV region, we still see $\pi \rightarrow \pi^*$ and $n \rightarrow \pi^*$, but also see new lower excited state by different types of transitions imparted by the metal center. Metal d–d transitions (670 nm), metal to ligand charge transfer (MLCT) transitions that define the near-visible region (450–500 nm), and ligand to metal charge transfer (LMCT) transitions (~330 nm) and combinations thereof. The existence of these charge-transfer transitions results in a large red-shift against H_2L and is consistent with the intense coloration usually exhibited by Cu(II) and Au(III) metal ligand complexes. All in all, the labelled spectrum illustrates how metal coordination changes the electronic structure and creates MLCT, LMCT, and d–d bands, allowing absorption to extend further into the visible region and increase optical activity over the organic ligand alone. The TD-DFT study of the H_2L/Au complex reveals a succession of low-energy excited states that impart the optical and electronic properties of the material. The resulting UV-vis spectrum, based on superimposed Gaussian broadening of discrete transitions from the excited-state table, shows broad absorption bands from approximately 200 to 800 nm. The excited-state table contains transitions that primarily occur in three regions: weak, low energy bands stretching between 500 and 700 nm originating from the d–d transitions involving d-orbitals on the Au center; medium intensity transitions from the 350 to 500 nm region primarily arising from metal–ligand charge transfer (MLCT/LMCT) transitions; and strong, higher energy features below 350 nm, belonging to π–π^* excitations localized on the ligand framework. Each transition is defined by its excitation energy (eV), expectedly corresponding to its wavelength (nm) and its oscillator strength (*f*), which expresses the relative probability of the transition occurring. Based on the molecular orbital data, the HOMO is around 5.0 eV and the LUMO is around −1.8 eV; thus, the approximate size of the HOMO–LUMO energy gap is 3.2 eV, which correlates nicely to the most intense absorption in the UV region. The HOMO is metal-centered (Au d-character) and the LUMO ligand-centered, further reinforcing the assignment of MLCT transitions. The set of occupied orbitals is followed by deep bonding states at −15 eV to the HOMO, while the virtual orbital set

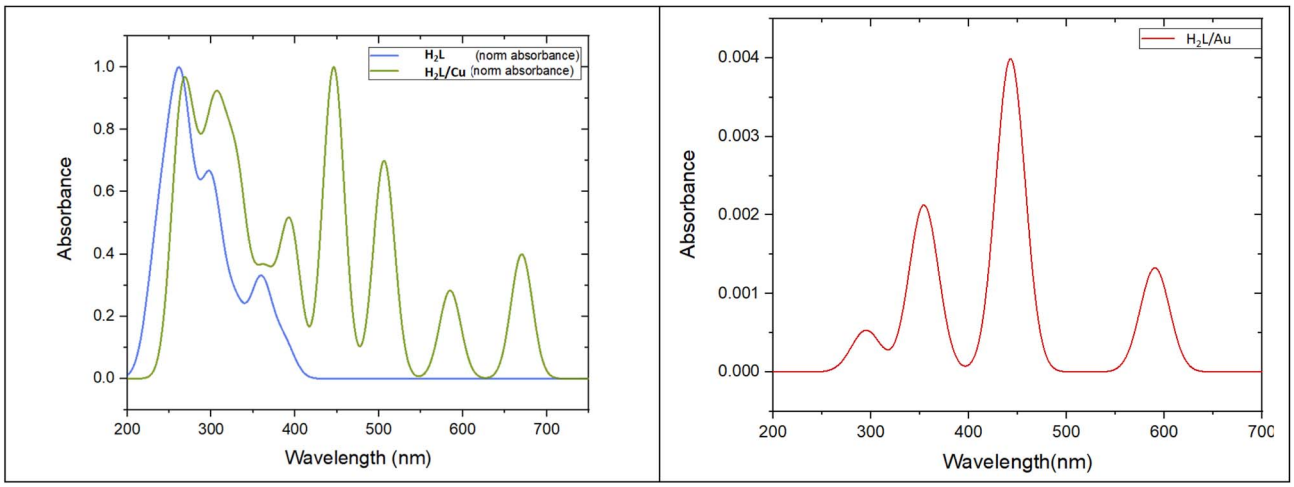

Fig. 11 TD-DFT of H_2L ligand, H_2L/Cu and H_2L/Au metal complexes.

Table 7 Thermodynamics analysis of H_2L ligand and metal chelates

Property	H_2L (kJ mol^{-1})	Cu complex (kJ mol^{-1})	Au complex (kJ mol^{-1})
E_0 + ZPE	−1 429 759.5	−2 139 865.4	−2 140 504.7
E_0 + thermal energy	−1 429 725.2	−2 139 430.8	−2 139 465.3
E_0 + enthalpy (H)	−1 429 722.6	−2 139 428.2	−2 139 462.8
E_0 + Gibbs free energy (G)	−1 429 865.2	−2 139 980.6	−2 140 859.9

follows to +4–5 eV, indicating the presence of a dense manifold of states that can be accessed upon excitation. In conclusion, the TD-DFT results have shown that the Au complex has a complex photophysical character that contains primarily charge-transfer excitations, with less contribution by ligand π–π* and metal d–d transitions. These characteristics suggest that H_2L/Au complex is a viable candidate for optical and catalytic applications, where visible-light absorption and frontier orbital alignment are critical design considerations.[69,70]

3.9.5. Thermodynamics investigation of H_2L ligand and its metal complexes. The thermodynamic study of the Schiff base ligand (H_2L) and its H_2L/Cu(II) and H_2L/Au(III) complexes give information about their relative stabilities and bonding features. The calculations were carried out with DFT/B3LYP/LANL2DZ at 298.15 K and 1 atm, and the results are given in the corrected Table 7 below.[62,63]

These revised quantities are well-suited to distinguish between the two metal complexes, and they incorporate the energetics in terms of actual energy differences. The H_2L/Au(III) complex having the more negative Gibbs free energy ($\Delta G \approx -2$ 140 859.9 kJ mol^{-1}) indicates that it is significantly more exothermic, and energetically competent when compared to the H_2L/Cu(II) complex ($\Delta G \approx -2$ 139 980.6 kJ mol^{-1}). The magnitude of the gold complex was ($\approx$880 kJ mol^{-1}) which relativistic stabilization of the 6s orbital and the 5d orbitals in Au(III) leads to enhanced Au-ligand covalency, resulting in stronger bonds. (2) Back-bonding interactions from filled d-orbitals lead to strong Au–S and Au–N bonds through overlap between metal d-orbitals and empty ligand π-antibonding orbitals. (3) As a result of the relativistic effects, Au(III) has a greater charge that makes Au(III) and its ligands more polarizable, allowing for improved charge delocalization and thus energy dissipation upon complexation and stabilization. Lastly, (4) there is an entropy and vibrational contribution; the H_2L/Au complex has larger ZPE and thermal corrections which showcase stronger interacting bonds and more substantial coupling. In context, while the H_2L/Cu(II) complex is more stable energetically, it has fewer negative values and therefore a slightly higher Gibbs energy. The less prominence of the energetic interactions based on less d–π overlap and less relativistic contribution manifests in a bond character more ionic in nature and energetically less stable. $H_2L < [Cu(H_2L)(H_2O)] < [Au(H_2L)(Cl_2)]$, This observation is in perfect accord with experimental observations: H_2L/Au(III) complex exhibits better XRD crystallinity, better SEM morphology rigidity, and less charge transfer resistance in electrochemical. These observations together suggest that H_2L/Au(III) complex is the most thermodynamically and kinetic stability, hence the best option for catalytic, electrochemical and sensory use. This observation is in perfect accord with experimental observations: H_2L/Au(III) complex exhibits better XRD crystallinity, better SEM morphology rigidity, and less charge transfer resistance in electrochemical. These observations together suggest that H_2L/Au(III) complex is the most thermodynamically and kinetically stable, hence the best option for catalytic, electrochemical and sensory use.

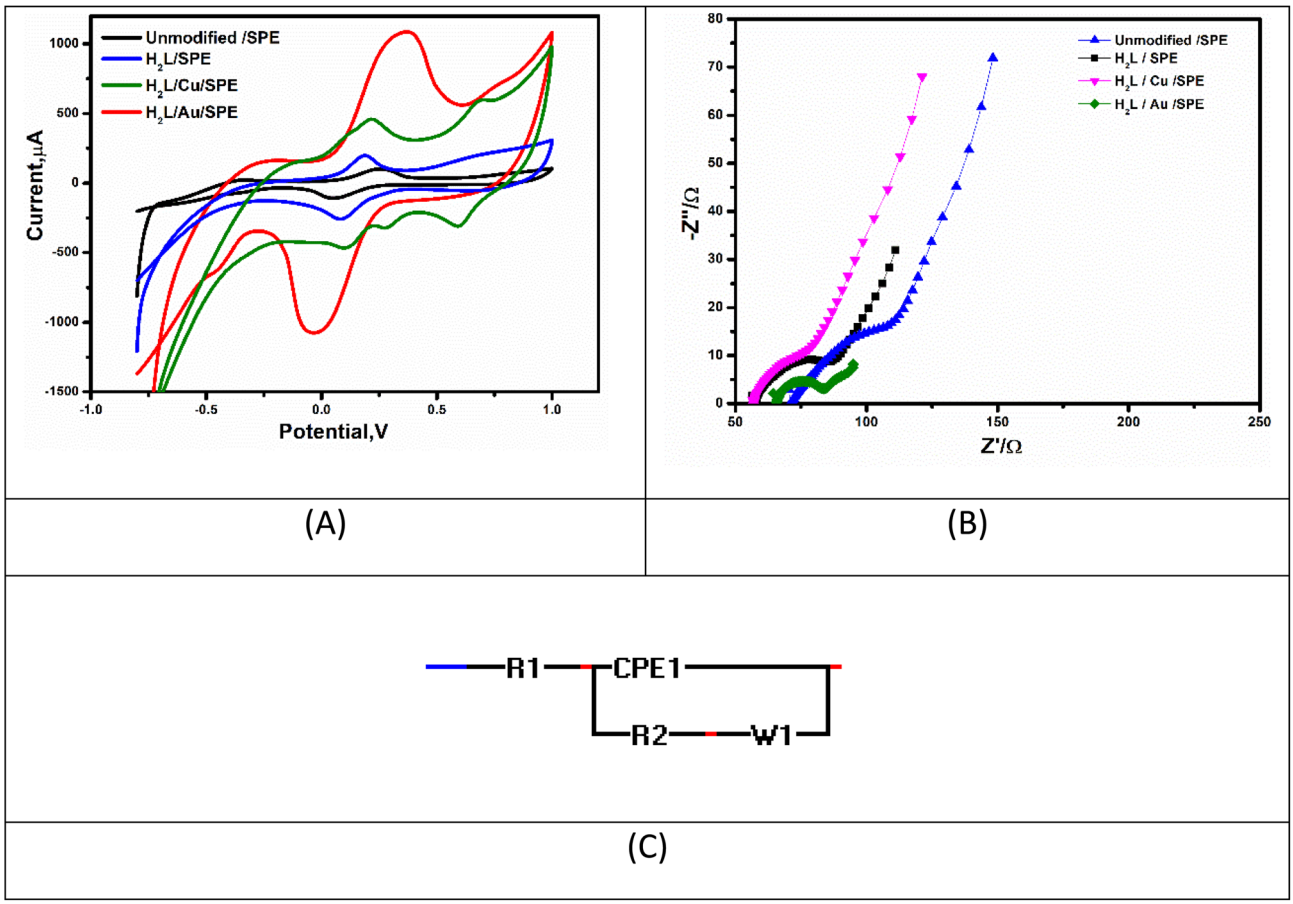

Fig. 12 (A) Cyclic voltammetry (CV) and (B) electrochemical impedance spectroscopy (EIS) measurements of unmodified SPE and modified SPEs with H_2L, H_2L/Cu and H_2L/Au, performed in a standard redox solution of ferro/ferricyanide in 0.1 M KCl at a scan rate of 50 mV s^{-1}. (C) Equivalent electrical circuit model used to fit the Nyquist plots from EIS data.

4. Applications of H_2L ligand and its metal complexes

4.1. Electrochemical properties

The electrochemical performance of bare (unmodified) screen-printed electrode (SPE) and H_2L, H_2L/Cu, and H_2L/Au modified SPEs was evaluated using cyclic voltammetry (CV) and electrochemical impedance spectroscopy (EIS). Measurements were conducted in a solution of 5 mM ferro/ferricyanide and 0.1 M KCl as the supporting electrolyte. Fig. 12A displays the cyclic voltammograms of all screen-printed electrodes (SPEs). The modified electrodes exhibited rapid and enhanced faradaic currents. A progressive increase in faradaic current was observed for H_2L/Cu and H_2L/Au modified SPE, attributed to improved electrical conductivity imparted by metal (Cu or Au).Specifically, the unmodified electrode exhibited the lowest faradaic current (anodic peak current, $I_{pa} = 107.97$ μA; cathodic peak current, $I_{pc} = -113$ μA) at 0.251 V and 0.053 V, respectively. With H_2L, the currents increased ($I_{pa} = 203$ μA; $I_{pc} = -256$ μA) at 0.184 V and 0.076 V. The H_2L/Cu -modified SPE showed further enhancement ($I_{pa} = 466$ μA; $I_{pc} = -472$ μA) at 0.213 V and 0.109 V. The highest faradaic response was achieved for H_2L/Au modified SPE ($I_{pa} = 1118$ μA; $I_{pc} = -1082$ μA) at 0.374 V and −0.039 V. Quantitative electrochemical parameters, including I_{pa}, I_{pc}, E_{ox}, E_{red}, $E_1/_2$, R_{ct}, capacitance (C), and Warburg impedance (W) for all compositions, are summarized in Table 8. The Nyquist plots (Fig. 12B) show semicircles at high frequencies representing charge transfer resistance (R_{ct}) at the electrode–electrolyte interface. From the circuit which used for fitting the impedance data included resistance of solution (R_s), charge transfer resistance (R_{ct}), constant phase element (CPE) and Warburg impedance (W) (see Fig. 12C), the measured R_{ct} value for unmodified electrode was (79 Ω) then decreased for the surface modification with H_2L (42 Ω), H_2L/Cu (40 Ω) and H_2L/Au (19 Ω). This trend indicates enhanced electron transfer kinetics. Overall, the H_2L/Au -modified screen-printed electrode demonstrated the best electrochemical performance, making them promising candidates for advanced electrochemical applications.

To further investigate the electrochemically active surface area (ECSA)[26,27,71] of screen-printed electrodes (SPEs) modified with the synthesized H_2L, H_2L/Cu and H_2L/Au nanomaterials, as well as the unmodified SPE, voltammetric experiments were carried out at varying scan rates in a ferri/ferrocyanide (FCN), 0.1 M KCl solution. As shown in Fig. 13(A)–(D), all electrodes

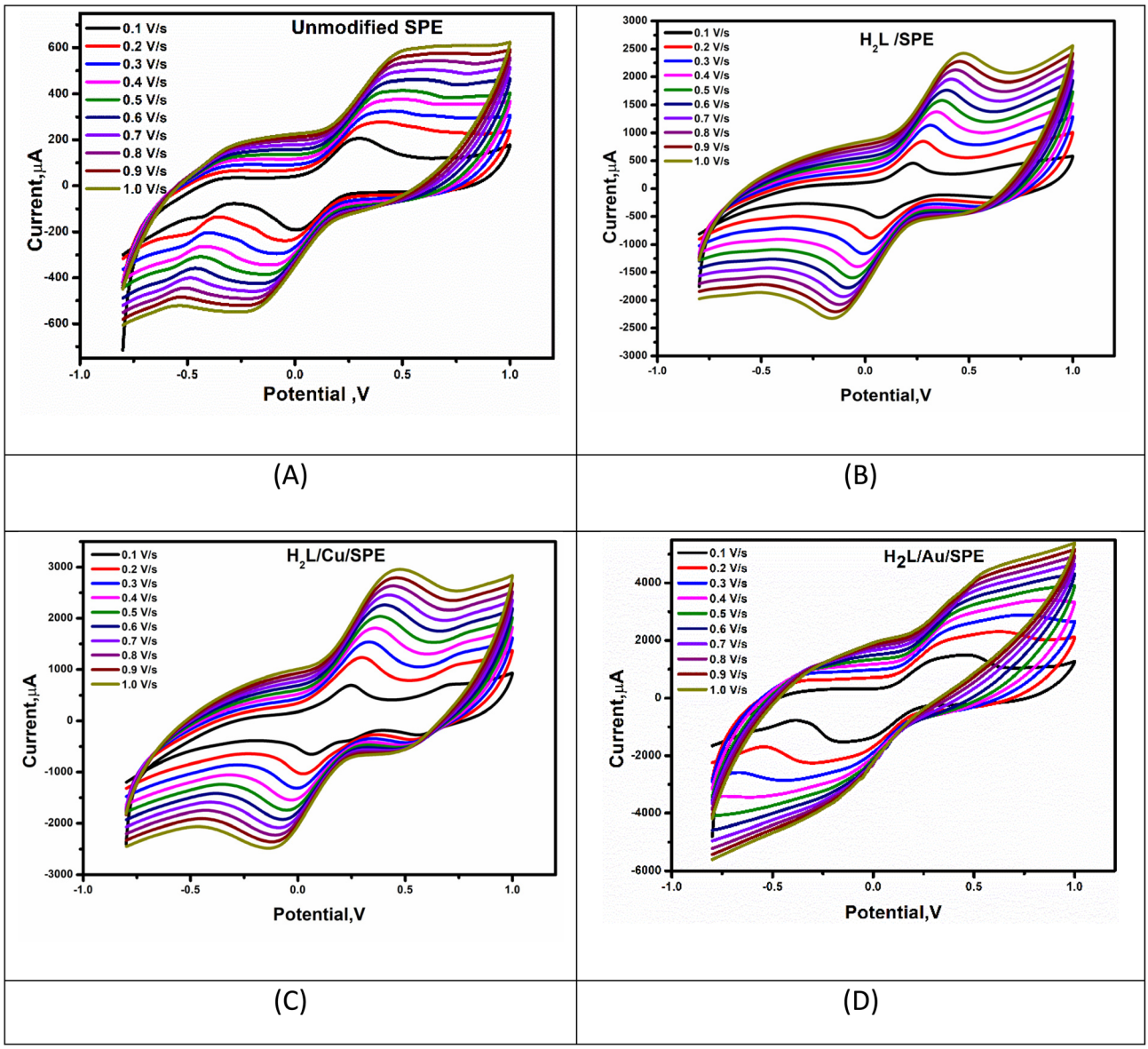

Fig. 13 (A–D) Cyclic voltammograms (CVs) of screen-printed electrodes (SPEs) modified with unmodified SPE H_2L, H_2L/Cu and H_2L/Au recorded at different scan rates.

Table 8 Summary of CV and EIS parameters obtained from experimental measurements (as shown in Fig. 12) for bare and modified SPE with the synthesized H_2L, H_2L/Cu and H_2L/Au nanomaterials[a]

Electrode type	I_{pa} (μA)	I_{pc} (μA)	$E_{oxd.}$ (V)	$E_{red.}$ (V)	$E_{1/2}$ (V)	R_s (Ω)	R_{ct} (1) (Ω)	CPE μF	n	W (Ω)	C_s (F g^{-1})
Bare (unmodified SPE)	107.97	−113	0.251	0.053	0.152	71.2	79.6	9.65	0.98	0.0057	774
H_2L/SPE	203	−256	0.184	0.076	0.13	58.6	42.8	12.3	0.91	0.0054	386
H_2L/Cu/SPE	466	−472	0.213	0.109	0.161	56.9	40.6	13.1	0.87	0.0048	250
H_2L/Au/SPE	1118	−1082	0.374	−0.039	0.167	65.8	19.1	20.5	0.95	0.0031	189

[a] I_a: anodic current, I_c: cathodic current, E_{oxd}: potential of oxidation, E_{red}: potential of reduction, R_s: solution resistance, R_{ct}: charge transfer resistance, CPE: constant phase element, W: Warburg resistance, C is specific capacitance of the electrodes at scan rate of 50 mV s^{-1}.

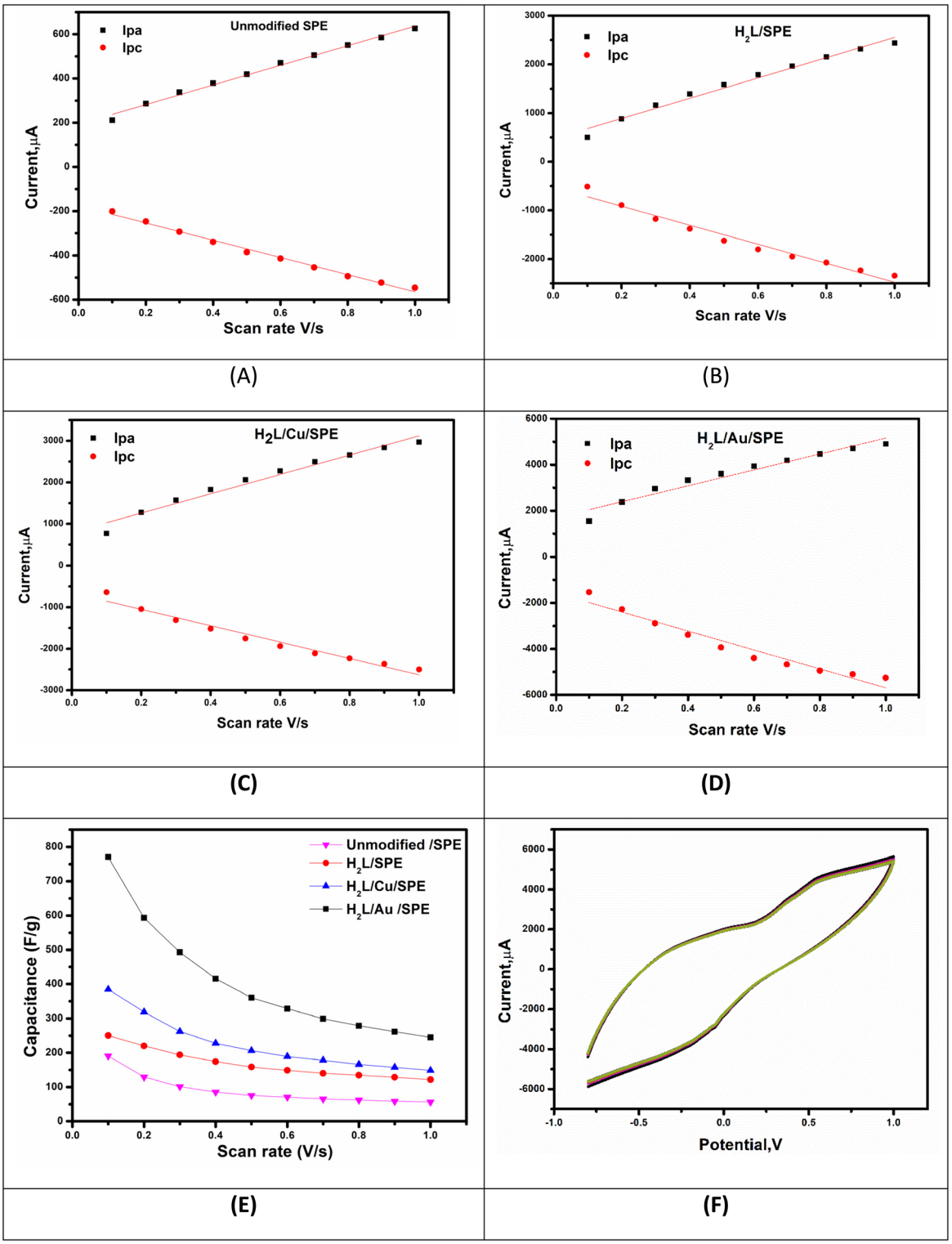

Fig. 14 (A–D) The graphs show the corresponding anodic (I_{pa}) and cathodic (I_{pc}) peak current plots *versus* the scan rate for unmodified SPE H_2L, H_2L/Cu and H_2L/Au modified SPE. (E) Specific capacitance values of the H_2L, H_2L/Cu and H_2L/Au modified SPEs at various scan rates. (F) The long-term cycling stability tests over 1000 cycles at scan rate 1 V s^{-1}.

exhibited a linear increase in redox peak current with increasing scan rate. Notably, the electrode modified with H_2L/Au demonstrated the most pronounced linear redox response.

The apparent saturation in the CV curves at higher scan rates may be attributed to diffusion limitations of the $[Fe(CN)_6]^{3-/4-}$ redox couple at the modified H_2L/Au/SPE surface. As the scan rate increases, the time available for redox species to diffuse to

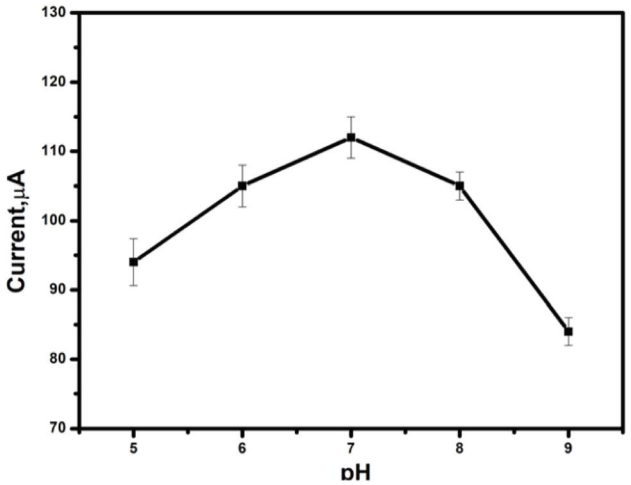

Fig. 15 The pH effect study on H_2L/Au – sensor performance towards the peroxide sensitivity.

the electrode surface decreases, which restricts the current response and leads to a saturation-like appearance. While capacitive contributions may play a secondary role due to the surface characteristics of the H_2L-modified electrode.

The electrochemically active surface area was estimated using the Randles–Ševčík equation:[27]

$$I_p = 2.69 \times 10^5 \times n^{3/2} \times A \times D^{1/2} \times Cu^{1/2} \quad (10)$$

where I_p is the peak current (A), n is the number of electrons transferred, D is the diffusion coefficient ($cm^2\ s^{-1}$), A is the electrochemically active surface area (cm^2), C is the concentration of FCN (mol L^{-1}), and ν is the scan rate (V s^{-1}). The anodic (I_{pa}) and cathodic (I_{pc}) peak currents were plotted against the scan rate, as shown in Fig. 14(A)–(D). A strong linear relationship was observed, with a correlation coefficient of 0.991. Using this data, the effective ECSA was calculated for the unmodified SPE and each modified variant. The unmodified SPE showed an active surface area of 0.19 cm^2, while the modified SPE with H_2L, H_2L/Cu and H_2L/Au exhibited a significantly larger surface area of 0.94, 1.06, 1.585 cm^2 respectively representing enhancement in the electrochemical active surface area. This substantial increase confirms the superior electrochemical performance of the H_2L/Au/modified electrode. Furthermore, the specific capacitance (C) was calculated using the following equation:

$$C = \frac{\int I\,dV}{2 \times \nu \times m \times \Delta V} \quad (11)$$

where C (F g^{-1}) is the specific capacitance, $\int I\,dV$ is the integrated area under the voltammetric curve, ΔV (V) is the potential window, m (g) is the mass of the active material, and ν (V s^{-1}) is the scan rate.All materials demonstrated excellent electrochemical stability across the range of applied scan rates, with no observable degradation or damage to the electrode structure. Significant improvements in electrochemical performance were observed upon modifying the electrode surface with H_2L, H_2L/Cu and H_2L/Au nanocomposites containing compared to the unmodified electrode. Among these, the H_2L/Au modified SPE exhibited the highest specific capacitance at all tested scan rates (see Fig. 14E and Table 8). At a scan rate of 50 mV s^{-1}, the specific capacitance for the H_2L/Au -modified electrode reached 774 F g^{-1}—substantially higher than that of the unmodified (189 F g^{-1}), H_2L (250 F g^{-1}) and H_2L/Cu (774 F g^{-1}).To evaluate the long-term electrochemical stability of the synthesized electrode material, cyclic voltammetry (CV) measurements were performed over 1000 continuous cycles at a scan rate of 1.0 V s^{-1} in 5 mM $[Fe(CN)_6]^{3-/4-}$/0.1 M KCl electrolyte. The CV curves were recorded within the potential window of −0.8 to 1.0 V (*vs.* Ag/AgCl). As shown in Fig. 14F, the shape of the CV curves remained largely unchanged throughout the cycling process, indicating high structural and electrochemical stability. Furthermore, the integrated area under the CV curves was used to assess the capacitive retention. After 1000 cycles, the electrode retained approximately [96.8%] of its initial capacitance, demonstrating excellent long-term cycling performance. This result confirms the robust nature of the electrode material and its potential applicability in supercapacitor devices.

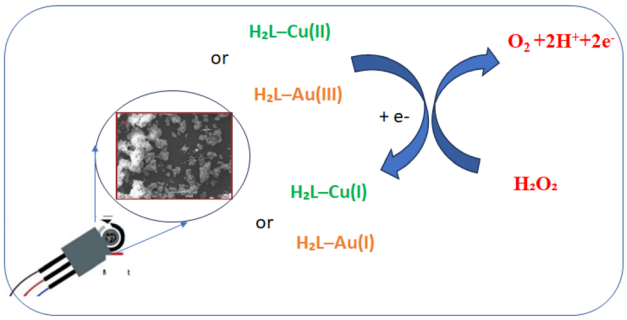

Scheme 3 A schematic diagram illustrate the mechanism of the H_2L/Cu and H_2L/Au modified electrodes for electrochemical detection of H_2O_2.

4.2. Peroxide detection

One of the key advantages of using metal–ligand complex[22] as electrode surface modifiers is their ability to provide strong electrocatalytic activity, facilitating rapid oxidation and efficient electron transfer in non-enzymatic peroxide sensors.[23,72–76] Consequently, all synthesized materials (H_2L/Cu and H_2L/Au) nanocomposites were evaluated for their direct electron transfer capabilities following peroxide oxidation.

4.2.1. Effect of pH. The pH of the supporting electrolyte significantly influences electrochemical performance.[25] The impact of pH variation on the amperometric response during peroxide oxidation was systematically evaluated. As shown in (Fig. 15), the response of the H_2L/Cu and H_2L/Au modified electrode to peroxide oxidation was examined across a range of pH levels. The electrical signal increased as the pH rose from 5.0 to 7.0, but declined at pH values of 8.0 and 9.0. Therefore, phosphate-buffered (PBS) at pH 7.0 was selected for all electrochemical measurements to provide a stable, physiologically relevant environment where the sensor exhibited optimal

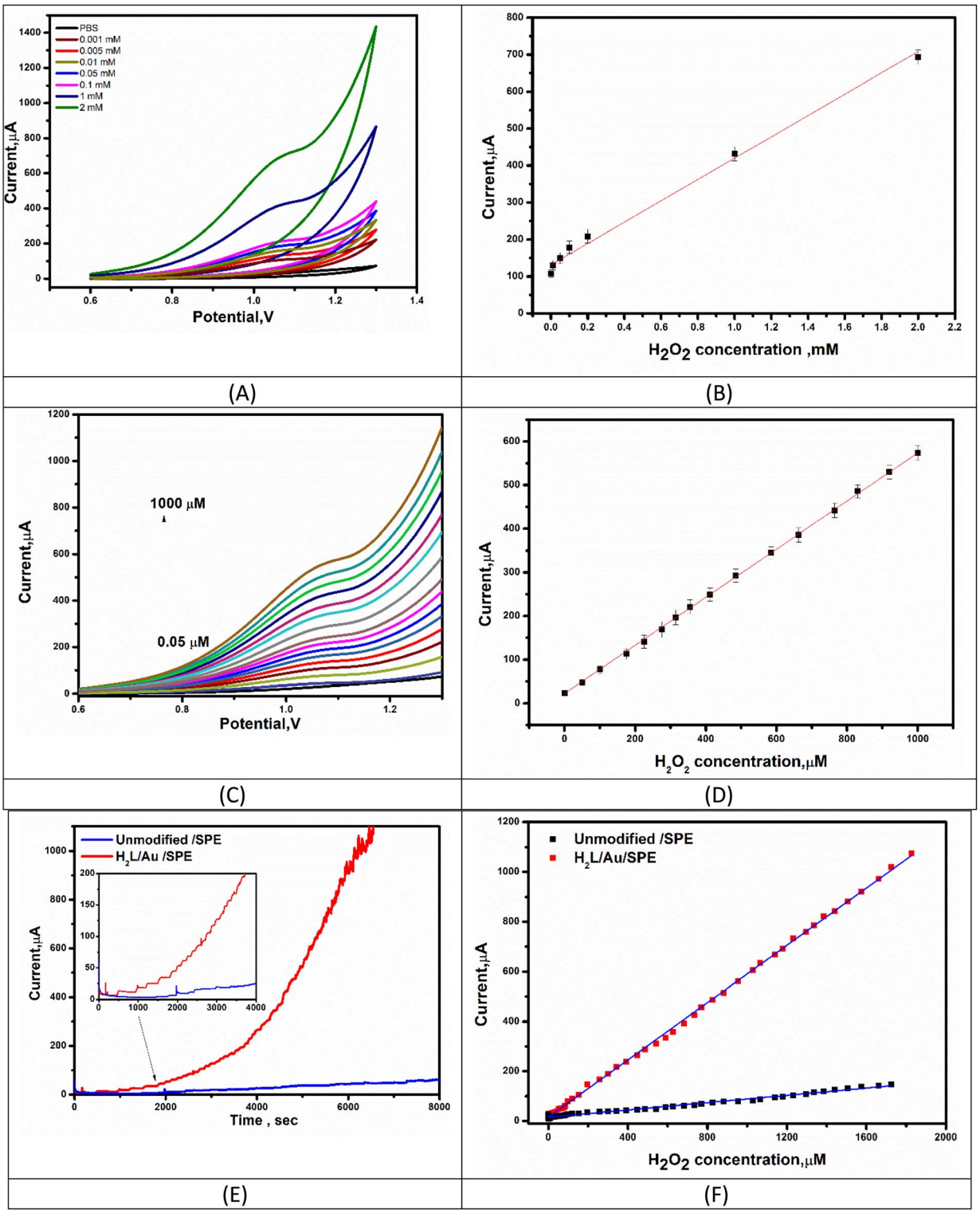

Fig. 16 (A) The cyclic voltammetry (CV) curves and its (B) linearity calibration curve. (C) The linear sweep voltammetry and (D) the linearity calibration curve. (E) The chronoamperometric and (F) The linearity calibration curve. Using unmodified, H_2L/Cu and H_2L/Au modified SPEs and solution containing PBS buffer and different concentration of H_2O_2.

stability and sensitivity. At higher pH values, decreased peak currents were observed due to reduced proton availability impacting proton-coupled electron transfer reactions, altered H_2O_2 stability, and possible changes in surface interactions, resulting in diminished electrocatalytic activity.

Based on these results, a PBS buffer with a pH of 7.0 was selected for all subsequent experiments.

4.2.2. Electrochemical detection for peroxide. Cyclic voltammetry (CV), square wave voltammetry (SWV), and chronoamperometry were performed using screen-printed electrodes (SPEs) modified with H_2L/Au, following the stepwise addition of H_2O_2. The resulting current responses (Fig. 16) demonstrated rapid and efficient electron transfer at the H_2L/Au-modified electrode surface. CV measurements revealed a high and fast response (Fig. 16A and B), with a wide linear detection range from 0.001 to 0.8 mM and a low detection limit (LOD) of 0.0005 mM (S/N = 5). Additionally, SWV exhibited a linear range from 0.05 μM to 1000 μM and an LOD of 0.003 μM (Fig. 16C and D).

Chronoamperometric detection of hydrogen peroxide (see Fig. 16E) using H_2L/Au-modified screen-printed electrode (SPE) was carried out by introducing a known amount of peroxide at a fixed time interval (50 seconds). The relationship between peroxide concentration and current response (Fig. 16F) demonstrated a rapid and strong signal for all modified SPEs, confirming efficient electron transfer with high sensitivity of 0.575 μA/μM featuring a wide linear detection range from 0.05 to 1725 μM and a low detection limit of 0.025 μM (S/N = 5). Compared to values reported in the literature,[25,29–31,77] this performance indicates that such modified materials are highly effective for use in enzymatic-based biosensor applications.

The superior performance of the H_2L/Au-modified screen-printed electrode (SPE) in hydrogen peroxide sensing can be attributed to higher electrical conductivity of Au(III) which facilitate rapid electron transfer at the electrode–analyte interface, stable and rigid molecular configuration of Au(III) complex which enhances the stability and reproducibility of the sensing surface. The increase in the effective electroactive surface area of the H_2L/Au-modified electrode which promote faster redox reactions with H_2O_2. The lower charge transfer resistance (R_{ct}) of H_2L/Au-modified electrode compared to H_2L/Cu and the bare SPE, indicating improved charge transfer properties and enhanced the sensing performance.

4.2.3. The proposed electrochemical detection mechanism for H_2O_2. The electrochemical detection of H_2O_2 by the H_2L/Cu and H_2L/Au modified electrodes is believed to follow a redox-mediated electrocatalytic mechanism. The metal centers (Cu^{2+} and Au^{3+}) facilitate electron transfer through reversible redox cycling (*e.g.*, Cu^{2+}/Cu^{+} or Au^{3+}/Au^{1+}), which in turn promotes the catalytic reduction of hydrogen peroxide. The Schiff base ligand framework enhances the electron transfer efficiency *via* π-conjugation and metal coordination, providing a stable and conductive environment for catalytic activity. The overall mechanism leads to an amplified current response, consistent with the observed high sensitivity of the modified electrodes toward H_2O_2 detection.

The Schiff base ligand coordinates to the metal centers (Cu(II) and Au(III)) *via* nitrogen and oxygen donor atoms, forming stable complexes. These metal centers serve as active sites for H_2O_2 adsorption and catalysis, facilitating effective interaction between the analyte and the sensor surface. Upon exposure to H_2O_2, the metal center undergoes redox cycling Cu(II) is reduced to Cu(I) and Au(III) is reduced to Au(I) through electron transfer facilitated by the applied potential. This redox activity promotes the catalytic decomposition or reduction of H_2O_2, generating a measurable current proportional to its concentration. The selective binding and catalytic activity arise from the specific coordination environment of the metal centers, which favor H_2O_2 interaction over other potential interfering species. The molecular structure of the Schiff base also provides steric and electronic environments that enhance selective electron transfer kinetics (Scheme 3).

Table 9 Determination of peroxide in real samples

Sample	H_2O_2 concentration added	H_2O_2 concentration found (μM)	Recovery %
Water	400 μM	397 ± 5.0	100.7
	800 μM	798 ± 4.0	100.2
Milk	200 μM	200.2 ± 3.1	99.9
	400 μM	400.6 ± 2.1	99.8
Cheese	400 μM	398 ± 2.3	100.5
	800 μM	798 ± 3.6	100.2
Salami	300 μM	295 ± 5.6	101.6
	400 μM	398 ± 2.5	100.5
Orange juice	500 μM	4.0 ± 496	125.0
	600 μM	599 ± 2.0	100.1

4.3. Application of peroxide detection in real samples

For practical applications, the amount of peroxide in water, milk, cheese, salami and juice was measured by the chronoamperometric (CA) technique and the modified electrode. A standard addition method was applied for peroxide detection in the real samples. The H_2O_2 concentration "Found" values represent the experimentally determined concentrations of hydrogen peroxide obtained using the developed sensor during recovery experiments. They were calculated based on the sensor's calibration curve by correlating the measured current response to the corresponding H_2O_2 concentration. The peak current measurements performed by the CA technique were compared with the calibration linear plot (presented in Fig. 16) to accurately determine the concentration of peroxide. The good recovery of the samples, as presented in Table 9, confirmed the successful applicability of the H_2L/Au modified SPE for peroxide detection in food samples.[78]

5. Conclusion

In this study, a novel Schiff base ligand, (*E*)-2-((1*H*-pyrrol-2-yl) methyleneamino) benzenethiol (H_2L), and it's Cu(II) and Au(III) complexes were synthesized and fully characterized *via* elemental analysis, FT-IR, NMR, UV-vis spectroscopy, XRD, SEM, TGA/DTA and conductance measurements. The electronic structures, reactivity parameters and charge distribution of complexes were elucidated using computational studies (DFT/TD-DFT) which showed the high electrophillicity and strong charge-transfer character in the Au(III) complex compared to Cu(II) complex. Electrochemical studies of H_2L/Cu(II) or Au(III) complexes showing increase in the current, decreased charge transfer resistance and lower scatter with no effect on specific

capacitance. H_2L/Au exhibited the most favorable reaction kinetics and charge transfer properties for supercapacitor applications. Further, electrode modification with H_2L/Au electrochemically resulted in excellent electrocatalytic activity with regard to hydrogen peroxide detection, indicating wide linear ranges, excellent stability, and low detection limits. The detection of hydrogen peroxide *via* modification of the electrode using H_2L/Au has been demonstrated practically with real samples, including water, milk, cheese, salami, and juice to show H_2L/Au was a successful non-enzymatic H_2O_2 sensor. Therefore, the combined use of Schiff base chemistry and coordination with Cu(II) and Au(III) led to multifunctional nanocomposites with structural stability and improved electrochemical performance. The results support the potential application of such complexes in next-generation energy storage applications and ultra-sensitive electrochemical sensors.

Conflicts of interest

The authors declare that there is no conflict of interest.

Data availability

The authors confirm that the data supporting the findings of this study are available within the article.

References

1 S. A. Hosseini-Yazdi, P. Samadzadeh-Aghdam, A. Mirzaahmadi, A. A. Khandar, G. Mahmoudi, M. Ruck, T. Doert, S. S. Balula and L. Cunha-Silva, Synthesis, crystal structures, spectroscopic and electrochemical studies on Cu (II) and Ni (II) complexes with compartmental nitrogen–oxygen mixed donor ligands, *Polyhedron*, 2014, **80**, 41–46.

2 J. Anacona and J. Santaella, Synthesis, magnetic and spectroscopic studies of a Schiff base derived from cephaclor and 1, 2-diaminobenzene and its transition metal complexes, *Spectrochim. Acta, Part A*, 2013, **115**, 800–804.

3 S. Zolezzi, E. Spodine and A. Decinti, Electrochemical studies of copper (II) complexes with Schiff-base ligands, *Polyhedron*, 2002, **21**, 55–59.

4 M. A. Ayoub, Synthesis, spectroscopic, thermal, fluorescence properties and molecular modeling of novel Pt (II) complex with schiff base containing NS donor atoms, *J. Mol. Struct.*, 2018, **1173**, 17–25.

5 A. M. Fahim, H. S. Magar and M. A. Ayoub, Synthesis, characterization, thermal studies, electrochemical behavior, antimicrobial, docking studies, and computational simulation of triazole-thiol metal complexes, *Appl. Organomet. Chem.*, 2022, **36**, e6647.

6 C. Boulechfar, H. Ferkous, A. Delimi, A. Djedouani, A. Kahlouche, A. Boublia, A. S. Darwish, T. Lemaoui, R. Verma and Y. Benguerba, Schiff bases and their metal Complexes: A review on the history, synthesis, and applications, *Inorg. Chem. Commun.*, 2023, **150**, 110451.

7 M. A. Ayoub, E. H. Abd-Elnasser, M. A. Ahmed and M. G. Rizk, Novel (E)— 2-((1-(thiophen-2-yl) ethylidene)-amino) phenol Manganese (II) as an Ionophore Based on Thiocyanate-Selective Electrodes and Its Applications, *ECS J. Solid State Sci. Technol.*, 2023, **12**, 027002.

8 A. Kanwal, B. Parveen, R. Ashraf, N. Haider and K. G. Ali, A review on synthesis and applications of some selected Schiff bases with their transition metal complexes, *J. Coord. Chem.*, 2022, **75**, 2533–2556.

9 A. R. Mahfouz, H. G. Nada, H. S. Magar, K. Z. ElBaghdady and R. Y. A. Hassan, Nano-biosensors for rapid detection of antibiotic resistance genes blaCTX-M in Escherichia coli and blaKPC in Klebsiella pneumoniae, *Int. J. Biol. Macromol.*, 2025, **310**, 143216.

10 M. S. Hashem and H. S. Magar, Inventive pectic acid grafted with polyacrylamide for a highly sensitive and selective non-enzymatic dopamine sensor in pharmaceutical samples, *RSC Adv.*, 2025, **40**, 33758–33772.

11 B. Chandran, S. Ramasamy, S. K. Ponnaiah, E. Arumugam, S. Chandrasekaran, S. Karuppaiah and A. Ganesan, Cerium Zirconium Oxide-Decorated Reduced Graphene Oxide Nanocomposite for Low Potential Voltammetric Detection of N-Hydroxysuccinimide, *ACS Appl. Nano Mater.*, 2024, **7**, 6839–6850.

12 C. Bhuvaneswari, R. Shanmugam, A. Elangovan, P. Sathish Kumar, C. Sharmila, K. Sudha, G. Arivazhagan and P. Subramanian, Voltammetric nano-molar range quantification of agrochemical pesticide using needle-like strontium pyrophosphate embedded on sulfur doped graphitic carbon nitride electrocatalyst, *Food Chem.*, 2024, **437**, 137874.

13 M. S. Hashem and H. S. Magar, Creative synthesis of pH-dependent nanoporous pectic acid grafted with acrylamide and acrylic acid copolymer as an ultrasensitive and selective riboflavin electrochemical sensor in real samples, *Int. J. Biol. Macromol.*, 2024, **280**, 136022.

14 H. S. Magar, H. Abdelghany, M. N. Abbas, U. Bilitewski and R. Y. A. Hassan, Fast analysis of Staphylococcus aureus in food products using disposable label-free nano-electrochemical immunosensor chips, *Microchem. J.*, 2023, **193**, 109097.

15 H. S. Magar, P. K. Brahman and R. Y. A. Hassan, Disposable impedimetric nano-immunochips for the early and rapid diagnosis of Vitamin-D deficiency, *Biosens. Bioelectron.:X*, 2022, **10**, 100124.

16 H. S. Magar, A. M. El Nahrawy, R. Y. A. Hassan and A. B. Abou Hammad, Nanohexagonal iron barium titanate nanoparticles surface-modified NiFe2O4 composite screen-printed electrode for enzymatic glucose monitoring, *RSC Adv.*, 2024, **14**, 34948–34963.

17 H. S. Magar, A. M. Fahim and M. S. Hashem, Accurate, affordable, and easy electrochemical detection of ascorbic acid in fresh fruit juices and pharmaceutical samples using an electroactive gelatin sulfonamide, *RSC Adv.*, 2024, **14**, 39820–39832.

18 H. S. Magar, M. Fayez, F. Febbraio and R. Y. A. Hassan, Esterase-2 mutant-based nanostructured amperometric

biosensors for the selective determination of paraoxon (Neurotoxin), *Anal. Biochem.*, 2025, **698**, 115751.

19 H. S. Magar, R. Y. A. Hassan and M. N. Abbas, Non-enzymatic disposable electrochemical sensors based on CuO/Co_3O_4@MWCNTs nanocomposite modified screen-printed electrode for the direct determination of urea, *Sci. Rep.*, 2023, **13**, 2034.

20 H. S. Magar, R. Y. A. Hassan and A. Mulchandani, Electrochemical Impedance Spectroscopy (EIS): Principles, Construction, and Biosensing Applications, *Sensors*, 2021, **21**, 6578.

21 H. S. Magar, B. A. Hemdan, H. R. M. Rashdan and R. Y. A. Hassan, Rapid and Selective Detection of Foodborne Pathogens Using a Disposable Bio-sensing System Designed by Stepwise Antibody Immobilization on AuNPs@Cu-MOF Nanocomposite, *Journal of Analysis and Testing*, 2024, **8**, 478–492.

22 H. S. Magar, E. E. A. E. Magd, R. Y. A. Hassan and A. M. Fahim, Rapid impedimetric detection of cadmium ions using Nanocellulose/ligand/nanocomposite (CNT/Co_3O_4), *Microchem. J.*, 2022, **182**(107885).

23 H. A. S. Tohamy and H. S. Magar, ECS Journal of Solid State Science and TechnologyA Flexible, Low-Cost, Disposable Non-Enzymatic Electrochemical Sensor Based on MnO_2/Cellulose Nanostructure, *ECS J. Solid State Sci. Technol.*, 2022, **11**, 127003.

24 N. Yousf, E. Ouda, H. S. Magar, R. Y. A. Hassan, S. A. Mansour and E. S. M. Duraia, Synthesis, Characterization, and Electrochemical Sensing Applications of Bimetallic Oxide/Carbon Nanomaterials Hybrids, *J. Electrochem. Soc.*, 2022, **169**, 047518.

25 H. S. Magar, E. S. M. Duraia and R. Y. A. Hassan, Dopamine fast determination in pharmaceutical products using disposable printed electrodes modified with bimetal oxides carbon nanotubes nanocomposite, *Sci. Rep.*, 2025, **15**, 11229.

26 R. A. Sobh and H. S. Magar, Innovative formulation of a functional nano-copolymer derived from glycidyl methacrylate and acrylonitrile as an exceptionally sensitive and selective electrochemical sensor for folic acid detection in pharmaceutical and food samples, *Nanoscale*, 2025, **17**, 18359–18376.

27 H. S. Magar and A. M. Fahim, Sensing platform based on RGO/cellulose-triazole composite for the electrochemical detection of mercury (II) ions in food samples, *Microchem. J.*, 2025, **215**, 114243.

28 M. S. Hashem, H. S. Magar, A. M. Fahim and R. A. Sobh, Antimicrobial, antioxidant, mechanistic, docking simulation, and electrochemical studies for grafting polymerization of novel sulphonated gelatin derived from chicken feet, *Mater. Chem. Phys.*, 2023, **310**, 128474.

29 M. S. Hashem, H. S. Magar, A. M. Fahim and R. A. Sobh, Antioxidant-rich brilliant polymeric nanocomposites for quick and efficient non-enzymatic hydrogen peroxide sensor, *RSC Adv.*, 2024, **14**, 13142–13156.

30 H. S. Magar, M. S. Hashem and R. A. Sobh, Design of metal oxide nanoparticles-embedded polymeric nanocomposites for hydrogen peroxide chronoamperometric sensor, *Polym. Compos.*, 2024, **45**, 3653–3665.

31 R. A. Sobh, H. S. Magar, H. A. A. E. Salam and H. E. Nasr, Acrylate polymeric nanocomposites embedded with transition metal triazole complexes: synthesis, characterization, and prospective implement as hydrogen peroxide sensors, *J. Nanopart. Res.*, 2024, **26**, 127.

32 P. S. Kumar, J. Bae, J. W. Roh, Y. Min and S. Lee, Enhanced voltage and capacitance in flexible supercapacitors using electrospun nanofiber electrolytes and CuNi2O3@N-Doped omnichannel carbon electrodes, *Nano Convergence*, 2025, **12**, 21.

33 J. Wang, *Electroanalytical techniques in clinical chemistry and laboratory medicine*, John Wiley & Sons, 1988.

34 P. Kissinger, P. T. Kissinger, W. R. Hieneman and W. R. Heineman, *Laboratory Techniques in Electroanalytical Chemistry, Revised and Expanded*, CRC press, 2018.

35 N. Turan, K. Buldurun, H. Seymen, B. Gündüz and N. Çolak, Opto-electronic studies and diode applications: synthesis, characterization, and photoconductive properties of Schiff base and its Pd (II) and Pt (II) complexes, *Res. Chem. Intermed.*, 2025, **51**, 1989–2005.

36 M. A. Ayoub, E. H. Abd-Elnasser, M. A.-A. Ahmed and M. G. Rizk, Synthesis, physicochemical, thermal, fluorescence and catalytic activity studies of novel Mn (II), Co (II), Ni (II) and Cu (II) complexes with tridentate (ONS) Schiff base ligand, *Eur. J. Chem.*, 2017, **8**, 85–95.

37 M. M. Więcław, tesliper: a theoretical spectroscopist's little helper, *J. Open Source Softw.*, 2022, **7**, 4164.

38 F. Weinhold and C. R. Landis, Natural bond orbitals and extentions of localized bonding concepts, *Chem. Educ. Res. Pract.*, 2001, **2**, 91–104.

39 A. Heidari, A. M. Fahim and M. H. Majd, Elucidating CT-DNA refolding and antitumor efficacy of novel phendione-Pd(II) complexes: A comprehensive computational and experimental study, *Int. J. Biol. Macromol.*, 2025, **327**, 147305.

40 K. Nakamoto, *Infrared and Raman Spectra of Inorganic and Coordination Compounds, Part B: Applications in Coordination, Organometallic, and Bioinorganic Chemistry*, John Wiley & Sons, 2009.

41 M. A. Ayoub, E. H. Abd-Elnasser, M. A. Ahmed and M. G. Rizk, Some new metal (II) complexes based on bis-Schiff base ligand derived from 2-acetylethiophine and 2, 6-diaminopyridine: Syntheses, structural investigation, thermal, fluorescence and catalytic activity studies, *J. Mol. Struct.*, 2018, **1163**, 379–387.

42 S. Chahmana, S. Keraghel, F. Benghanem, R. Ruíz-Rosas, A. Ourari and E. Morallón, Synthesis, spectroscopic characterization, electrochemical properties and biological activity of 1-[(4Hydroxyanilino)-methylidene] naphthalen-2 (1H)-one and its Mn (III) Complex, *Int. J. Electrochem. Sci.*, 2018, **13**, 175–195.

43 P. Kanmani, S. Rajalakshmi and M. Tamilselvi, Synthesis and spectral analysis of Mn (II), Co (II), Zn (II) and Cd (II) complexes of a new Schiff base derived from p-vanillin and 4-nitroaniline, *Adv. J. Chem., Sect. A*, 2016, **7**, 2229–5518.

44 L. Bellamy, *The Infra-red Spectra of Complex Molecules*, Springer Science & Business Media, 2013.
45 E. H. Abd Elnasser, M. A. Ayoub, M. A. Ahmed and G. Mariam, Synthesis and Characterization of N-(2-acetylthiophene) salicylideneimine (ATS) as Ionophore for Polymeric Membrane Ag (I) Selective Electrode, *Egypt. J. Chem.*, 2016, **59**, 1001–1012.
46 A. M. Fahim and M. G. Elbanna, A novel ruthenium(VI) benzylidene carbene complex: Synthesis, crystal structure, hirshfeld surface, electrochemical behavior, and DFT insights, *J. Mol. Struct.*, 2026, **1351**, 144381.
47 F. A. Cotton, G. Wilkinson, C. A. Murillo and M. Bochmann, *Advanced Inorganic Chemistry*, John Wiley & Sons, 1999.
48 B. D. Cullity and R. Smoluchowski, Elements of X-ray Diffraction, *Phys. Today*, 1957, **10**, 50.
49 L. H. Abdel-Rahman, S. F. Alzarzah, M. Abdel-Hameed, M. R. Shehata and A. El-Saghier, A new bio-active Schiff base ligand and its Ni (II), Cu (II), Ag (I), Zn (II), Cd (II), and La (III) binuclear complexes: synthesis, DFT analysis, antimicrobial, DNA interaction, COXII inhibition, and molecular docking studies, *Appl. Organomet. Chem.*, 2024, **38**, e7631.
50 H. Al-Maydama, A. El-Shekeil, M. A. Khalid and A. Al-Karbouly, Thermal degradation behaviour of some polydithiooxamide metal complexes, *Ecletica Quim. J.*, 2006, **31**, 45–52.
51 A. Frisch, *gaussian 09W Reference*, Wallingford, USA, 2009, p. 25.
52 A. M. Fahim and M. A. Shalaby, Synthesis, biological evaluation, molecular docking and DFT calculations of novel benzenesulfonamide derivatives, *J. Mol. Struct.*, 2019, **1176**, 408–421.
53 N. A. Kheder, A. M. Fahim, N. S. Mahmoud and K. M. Dawood, Unreported Biginelli product with potent antifungal activity: Synthesis, DFT insights, and docking simulation analysis, *J. Mol. Struct.*, 2025, **1330**, 141480.
54 H. E. M. Tolan, A. M. Fahim and E. H. I. Ismael, Synthesis, biological activities, molecular docking, theoretical calculations of some 1,3,4-oxadiazoles, 1,2,4-triazoles, and 1,2,4-triazolo[3,4-b]-1,3,4-thiadiazines derivatives, *J. Mol. Struct.*, 2023, **1283**, 135238.
55 P. K. Chattaraj, A. Cedillo and R. G. Parr, Chemical softness in model electronic systems: dependence on temperature and chemical potential, *Chem. Phys.*, 1996, **204**, 429–437.
56 W. Gordy and W. O. Thomas, Electronegativities of the elements, *J. Chem. Phys.*, 1956, **24**, 439–444.
57 A. Hanna and M. Tinkham, Variation of the Coulomb staircase in a two-junction system by fractional electron charge, *Phys. Rev. B*, 1991, **44**, 5919.
58 R. G. Parr and R. G. Pearson, Absolute hardness: companion parameter to absolute electronegativity, *J. Am. Chem. Soc.*, 1983, **105**, 7512–7516.
59 L. R. Domingo, M. J. Aurell, P. Pérez and R. Contreras, Quantitative characterization of the global electrophilicity power of common diene/dienophile pairs in Diels–Alder reactions, *Tetrahedron*, 2002, **58**, 4417–4423.
60 A. Vela and J. L. Gazquez, A relationship between the static dipole polarizability, the global softness, and the fukui function, *J. Am. Chem. Soc.*, 1990, **112**, 1490–1492.
61 A. Ino, T. Mizokawa, A. Fujimori, K. Tamasaku, H. Eisaki, S. Uchida, T. Kimura, T. Sasagawa and K. Kishio, Chemical potential shift in overdoped and underdoped La 2− x Sr x CuO 4, *Phys. Rev. Lett.*, 1997, **79**, 2101.
62 H. E. M. Tolan, E. H. I. Ismael, H. M. Awad and A. M. Fahim, New mercaptopyrimidine derivatives synthesized with expected antimicrobial and antioxidant properties and theoretical study, *J. Mol. Struct.*, 2025, **1324**, 140795.
63 M. A. Shalaby, A. M. Fahim and S. A. Rizk, Microwave-assisted synthesis, antioxidant activity, docking simulation, and DFT analysis of different heterocyclic compounds, *Sci. Rep.*, 2023, **13**, 4999.
64 G. H. Elsayed and A. M. Fahim, Studying the impact of chitosan salicylaldehyde/schiff base/CuFe2O4 in PC3 cells via theoretical studies and inhibition of PI3K/AKT/mTOR signalling, *Sci. Rep.*, 2025, **15**, 4129.
65 A. M. Fahim, Exploring novel benzene sulfonamide derivatives: Synthesis, ADME studies, anti-proliferative activity, docking simulation, and emphasizing theoretical investigations, *J. Indian Chem. Soc.*, 2024, **101**, 101211.
66 G. Abdel-Maksoud, A. M. Fahim and R. A. Sobh, Preliminary evaluation of green terpolymer of nano poly (methyl methacrylate/dimethylaminoethyl methacrylate/acrylamide) for the consolidation of bone artifacts, *Polym. Bull.*, 2025, **73**, 139–149.
67 G. H. Elsayed and A. M. Fahim, Synthesis, theoretical investigation, and anti-proliferative assessment of novel fused heterocyclic cellulosic derivatives in colorectal Caco-2 cells via suppressing the IL6/STAT3 pathway, *J. Mol. Struct.*, 2025, **1347**, 143045.
68 A. M. Fahim, S. A. Abdelhamid and T. A. Hameed, Antimicrobial, antioxidant activities and ADME studies of novel BaSnO3 sulphone cellulose with docking simulation, *J. Mol. Struct.*, 2025, **1325**, 140945.
69 A. Heidari, A. M. Fahim and M. H. Majd, Elucidating CT-DNA refolding and antitumor efficacy of novel phendione-Pd(II) complexes: A comprehensive computational and experimental study, *Int. J. Biol. Macromol.*, 2025, 147305.
70 H. S. Magar and A. M. Fahim, Sensing platform based on RGO/cellulose-triazole composite for the electrochemical detection of mercury (II) ions in food samples, *Microchem. J.*, 2025, **215**, 114243.
71 M. S. Hashem and H. S. Magar, Inventive pectic acid grafted with polyacrylamide for a highly sensitive and selective non-enzymatic dopamine sensor in pharmaceutical samples, *RSC Adv.*, 2025, **15**, 33758–33772.
72 A. B. A. Hammad, H. S. Magar, A. M. Mansour, R. Y. A. Hassan and A. M. E. Nahrawy, Construction and characterization of nano-oval BaTi0.7Fe0.3O3@NiFe2O4 nanocomposites as an effective platform for the determination of H2O2, *Sci. Rep.*, 2023, **13**, 9048.
73 E. Ouda, N. Yousf, H. S. Magar, R. Y. A. Hassan and E. S. M. Duraia, Electrochemical properties of MnO2-based carbon nanomaterials for energy storage and

electrochemical sensing, *J. Mater. Sci.: Mater. Electron.*, 2023, **34**, 731.

74 E. S. M. Duraia, B. M. Adebiyi, S. Das, H. S. Magar, G. W. Beall and R. Y. A. Hassan, Single-step synthesis of carbon nanotubes-nickel cobaltite (CNT-NiCo2O4) by thermal decomposition of cyanide compounds for electrochemical sensing applications, *Phys. E (Amsterdam, Neth.)*, 2024, **159**, 115902.

75 A. M. Mansour, H. S. Magar, A. Elzwawy, A. B. Abou Hammad and A. M. El Nahrawy, Structural, optical, and electrochemical properties of tungsten-doped cadmium zinc phosphate nanoporous materials for energy storage and peroxide detection, *RSC Adv.*, 2025, **15**, 15670–15693.

76 E. Ouda, N. Yousf, A. Elzwawy, H. S. Magar, R. Y. A. Hassan, M. El-Ashry and E. M. Duraia, Carbon nanotubes/lithium ferrite nanocomposites: magnetic and electrochemical optimization for enhanced H2O2 sensing, *RSC Adv.*, 2025, **15**, 33667–33681.

77 A. Elzwawy, A. M. Mansour, H. S. Magar, A. B. A. Hammad, R. Y. A. Hassan and A. M. El Nahrawy, Exploring the structural and electrochemical sensing of wide bandgap calcium phosphate/CuxFe3-xO4 core-shell nanoceramics for H2O2 detection, *Mater. Today Commun.*, 2022, **33**, 15670–15693.

78 B. Wang, H. Zhang, Y. Wen, W. Yuan, H. Chen, L. Lin, F. Guo, Z. P. Zheng and C. Zhao, The novel angiotensin-I-converting enzyme inhibitory peptides from Scomber japonicus muscle protein hydrolysates: QSAR-based screening, molecular docking, kinetic and stability studies, *Food Chem.*, 2024, **447**, 138873.